FERMILAB-MASTERS-2012-05

UNIVERSITÀ DEGLI STUDI DI ROMA "TOR VERGATA"

TESI DI LAUREA MAGISTRALE IN FISICA

———

Search for $W' \to tb$ in Events with Large Missing Transverse Energy and Jets with the CDF detector at the Fermilab Tevatron Collider

Advisors
Prof. Giorgio BELLETTINI
Prof. Anna DI CIACCIO

Candidate
Ludovico BIANCHI

Supervisor
Dr. Matteo CREMONESI

A. A. 2011/2012

UNIVERSITÀ DEGLI STUDI DI ROMA "TOR VERGATA"

TESI DI LAUREA MAGISTRALE IN FISICA

———

Ricerca di $W' \to tb$ in Eventi con Alta Energia Trasversa Mancante e Getti Adronici con l'Esperimento CDF al Tevatron

Relatori
Prof. Giorgio BELLETTINI
Prof. Anna DI CIACCIO

Candidato
Ludovico BIANCHI

Correlatore
Dr. Matteo CREMONESI

A. A. 2011/2012

Abstract

In the scope of the strong ongoing data analysis efforts of the `CDF` collaboration at Fermilab, we present a search for the production of massive W' bosons decaying to a top and a bottom quark in $p\bar{p}$ collisions at $\sqrt{s} = 1.96$ TeV. To perform this search, we select events with large Missing Transverse Energy plus two or three jets, in which the W generated from top decays leptonically, and either the e or μ is lost or the τ is reconstructed as a jet. A complete study of the selected sample is discussed, including the creation and subsequent optimization of a Neural Network-based multivariate tool to reject the QCD multijet background from the signal region. Finally, we perform a likelihood-based multichannel Bayesian fit procedure on the invariant transverse mass of the Missing Transverse Energy and jets to extract 95% CL limits on $\sigma(p\bar{p} \rightarrow W') \times \mathcal{B}(W' \rightarrow tb)$ for $M_{W'}$ = 200 GeV/c^2.

Sommario

Nell'ambito dell'intenso sforzo in analisi dati attualmente in corso da parte della collaborazione `CDF` a Fermilab, viene presentata una ricerca di produzione di bosoni W' massivi che decadono in un quark top e un quark bottom in collisioni $p\bar{p}$ a Tevatron. Per effettuare la ricerca, selezioniamo eventi con alta Energia Trasversa Mancante e due o tre getti adronici nello stato finale, in cui il W proveniente dal decadimento del quark top decade in leptoni, e il e o il μ non sono identificati, o il τ viene ricostruito come getto adronico. Viene discusso uno studio completo del campione di dati selezionato, inclusa la realizzazione e la successiva ottimizzazione di un strumento multivariato basato su una Rete Neurale per rigettare il fondo di multigetti QCD dalla regione di segnale. Per ultimo, una procedura di fit multicanale Bayesiana viene applicata alla distribuzione della massa invariante trasversa dell'Energia Trasversa Mancante e getti per estrarre limiti su $\sigma(p\bar{p} \to W') \times \mathcal{B}(W' \to tb)$ per $M_{W'} = 200$ GeV$/c^2$.

Contents

5 QCD multijet background rejection 109

6 Setting the Limits 121

List of Figures

List of Tables

Introduction

W' and Z' refer collectively to Beyond the Standard Model (BSM) particles that are heavier counterparts of the W and Z of the Standard Model. Searching for W' and Z' bosons provides a versatile tool to probe a broad spectrum of different BSM scenarios, since their existence is predicted by several theoretical models. Searches for W' and Z' have been performed in the past both at Tevatron and LHC, the only machines capable of producing such massive particles, setting upper limits on the production cross-section. These analyses are sensitive also to other massive resonances that share the same final states, so they can serve as a benchmark to search for other more elusive particles. For these reasons, updating the previous searches with the full CDF II dataset in order to set more stringent limits is very interesting, especially since CDF has higher sensitivity than LHC experiments for low W' and Z' masses.

For this analysis, we focus on a W' that decays to a top and a bottom quark, and the W from top decays leptonically, but either the lepton (electron or muon) is not identified, or the tau is reconstructed as a jet. We thus select events with large missing transverse energy ($\not{E}_T$) and jets with high transverse momentum (p_T) in the final state: this is known as the $\not{E}_T$ plus jets channel. This channel is complementary to the lepton plus jets channel, in which an identified high-p_T lepton is required along with missing transverse energy and jets. In recent years, the strategy of the CDF collaboration has been to carry out several analyses in the two channels simultaneously. Performing the same search in a statistically independent data sample provides an independent confirmation of the results; last, and more importantly, combining the results from the two separate channels a higher overall sensitivity can be obtained.

The absence of an identified lepton makes analyses in this channel more challenging. QCD multijet, in which the missing transverse energy is due to instrumental mismeasurements rather than being intrinsic of the physical process, is the main background process with a cross-section roughly 10^6 greater than the processes which are to be studied. This requires the implementation of ingenious techniques for background simulation and rejection in order to reach a high sensitivity.

This discussion is organized as follows. In Chapter 1, the theoretical framework of the thesis is set. First, a general description of the Standard Model is given. Then, an overview of the strategies for the search of W' and Z' bosons is presented, including a review of previous analyses and the features of the theoretical model used as a reference for this search.

A correct understanding of the experimental setup is mandatory for any scientific activity; for this reason, a rather detailed summary of the experimental apparatus is provided. Chapter 2 describes the Tevatron collider and the `CDF` detector, while Chapter 3 describes the techniques employed at `CDF` to reconstruct physical objects from detector information, with a particular focus on those most relevant for the scope of this analysis.

In Chapters 4 and 5 the main analysis is reported in detail: features of the datasets used in this analysis, signal and background modeling, preselection requirements, background rejection techniques and the main tools used to implement them are described.

During my stay at Fermilab, as a member of the `CDF` Top/BSM Physics Group, I had the opportunity to actively take part in all the stages of the analysis, including initial strategic planning, and and presenting periodical status reports on the progress of my work at group meetings. My initial effort was spent in learning and subsequently optimizing the analysis framework under the instructions of my supervisor. My work then focused on the creation and optimization of a multivariate tool, based on an Artificial Neural Network, to reject the QCD multijet background in the selected sample. Because of the overwhelmingly large contribution from this background process, a multivariate approach is essential to ensure high rejection performance without sacrificing signal efficiency. Then, we developed a novel way to estimate pre-fit normalization for QCD multijet and V + jets processes, improving the background modeling in the signal region and significantly reducing uncertainties on background contribution estimates. Eventually, in collaboration with my supervisor the final fit, which is described in Chapter 5, was performed. in this Chapter the adopted statistical techniques and the considered systematic uncertainties are also addressed.

Chapter 1

The Standard Model and the W'

As of now, our knowledge of Nature is based on the existence of four fundamental forces: gravitational, electromagnetic, weak and strong nuclear forces. Most of the efforts in theoretical physics are directed towards the unification of all interactions under a complete theory. Currently, three out of four (electromagnetic, weak and strong nuclear force) are included in a larger frame called *Standard Model* (SM) of the fundamental interactions. Since it does not include the gravitation in a complete ultimate theory, the search for a universal model is still ongoing.

The SM is an elegant and calculable theory that describes most of the elementary particle physics processes. It successfully predicted the existence of new particles later discovered in high-energy physics experiments, like the W and Z bosons and the top quark. In March 2013 the discovery of a new particle of mass about 125 GeV$/c^2$ was announced at CERN, with features as expected as the Higgs boson predicted in the Standard Model. Although not yet conclusive, the on-going studies to ascertain its nature seem to confirm that this particle is indeed the SM Higgs boson ([1, 2]).
A vast amount of different models, usually referred to as Physics Beyond the Standard Model (BSM), are being proposed to replace or extend the SM.

Currently, no experimental evidence of physics processes characterized by large discrepancies with SM expectations has been found.

1.1 Particles and Fields: a Gauge Theory

The SM is a quantum field theory in which particles are treated as local quantum fields interacting via the exchange of force mediators (each type of force has its own mediators), that are introduced in order to conserve local symmetries i.e. the theory has to be *gauge invariant* under local trasformations [3]. The SM is based on gauge symmetry group $\mathrm{SU}(3) \otimes \mathrm{SU}(2) \otimes \mathrm{U}(1)$: $\mathrm{SU}(3)$ describes QCD (Quantum-Chromo-Dynamics) theory of strong interactions, $\mathrm{SU}(2)$ describes weak theory and $\mathrm{U}(1)$ the QED (Quantum-Electro-Dynamics) theory of electromagnetism.

As summarized in table 1.1, elementary particles are divided in two fundamental groups by their spin: leptons and quarks, with half-integer spin, and bosons, with integer spin. Quarks and leptons follow Fermi-Dirac statistics and are called *fermions*, while *bosons* follow Bose-Einstein statistics.

1.1.1 Fermions

The matter, as we know so far, is built up by fermions that are divided in two classes: leptons and quarks. For each fermion exists a corresponding anti-particle with same mass and opposite quantum numbers. Each class can be ordered in three generations, also called *families* (see table 1.1). Only first generation particles can form stable matter, while second and third generations fermions are created by high energy processes and subsequently decay into first generation states.

Quarks exist in six different types, called *flavors*, as shown in table 1.1, with a fractional electric charge of 2/3 and -1/3. They interact through EM,

	Name	Symbol	Spin ($\hbar$)	Charge (e)	Mass (MeV/c^2)
Leptons	e neutrino	ν_e	1/2	0	$< 2 \cdot 10^{-6}$
	electron	e	1/2	-1	$0.510998910 \pm 0.000000013$
	μ neutrino	ν_μ	1/2	0	< 0.19
	muon	μ	1/2	-1	$105.6583668 \pm 0.0000038$
	τ neutrino	ν_τ	1/2	0	< 18.2
	tau	τ	1/2	-1	1776.82 ± 0.16
Quarks	up	u	1/2	2/3	$2.49\pm^{0.81}_{0.79}$
	down	d	1/2	-1/3	$5.5\pm^{0.75}_{0.95}$
	charm	c	1/2	2/3	$(1.27\pm^{0.07}_{0.09}) \cdot 10^3$
	strange	s	1/2	-1/3	$101\pm^{29}_{31}$
	beauty	b	1/2	2/3	$(4.19\pm^{0.18}_{0.06}) \cdot 10^3$
	top	t	1/2	-1/3	$(172.0\pm^{0.9}_{1.3}) \cdot 10^3$
Gauge Bosons	photon	γ	1	0	0
	W boson	$W^{\pm}$	1	± 1	$(80.399 \pm 0.023) \cdot 10^3$
	Z boson	Z^0	1	0	$(91.1876 \pm 0.0021) \cdot 10^3$
	gluon	g	1	0	0

Table 1.1 – Elementary particles in the SM and their properties (from [4]).

weak and strong interaction. Quarks can be arranged by strong interaction in bound states, called hadrons, of $q\bar{q}$ pairs (mesons) or three quarks (baryons). Pauli's principle prohibits fermions in the same state, therefore quarks must have a new quantum number, that is called *color* flavor and results in three different types: red, yellow, blue. Bound states of quarks are color-neutral. Gluons, the strong force mediators, carry the color number itself, hence are self-coupled. This causes an increase of the force strength with the distance, so that quarks are tightly forced to be bound in hadrons (*confinement*) and they cannot be observed free.

Leptons interact via weak force and, if they carry electric charge, also via EM. They carry a *leptonic* number that characterizes each family. Neutrinos were originally assumed as massless while several measurement showed the presence of non-zero mass [5, 6]. So far, no direct measurement of ν mass exists [4].

1.1.2 Bosons and interactions

Interactions between particles in SM are mediated by spin-1 particles called bosons: photon (γ) mediates electromagnetic interaction, the $W^{\pm}$ and Z^0 mediates weak interaction and color-carrying gluons (g) mediates strong interactions. Those particles are needed in the SM in order to maintain local invariance of the Lagrangian density function of the physical system. In fact, local phase transformations of the free Lagrangian density produce the need of introducing gauge fields (i.e. the gauge bosons) to preserve local-gauge invariance. The invariance can be seen as a symmetry of the function and, according to Noether's theorem, when a symmetry is introduced in the system a conserved current verifying continuity equation is induced:

$$\partial_\mu J^\mu = 0 \tag{1.1}$$

Since the conservation of a current is associated with conservation of a charge (the time-component J^0 of 4-vector J^μ integrated over the space), it means that each interaction force has to conserve a quantum number: the electric charge Q in EM, the weak isospin charge I_3^W(and the associated weak hypercharge $Y = Q/e - I_3^W$) in weak interaction and color charge C_q in strong interaction [7]. Coupling with those charges, the gauge fields generates the interactions with strengths characterized by coupling constants with approximate relative magnitudes:

$$\alpha_{strong} : \alpha_{em} : \alpha_{weak} \approx \frac{1}{10} : \frac{1}{100} : \frac{1}{10000} \tag{1.2}$$

Typical lifetimes of processes belonging to those interactions are (in seconds):

$$\tau_{\text{strong}} \approx 10^{-23}, \quad \tau_{\text{em}} \approx 10^{-20} - 10^{-16}, \quad \tau_{\text{weak}} \approx 10^{-12} \tag{1.3}$$

Quantum Electrodynamics

The quantum field theory of electromagnetism is quantum electrodynamics (QED). The Lagrangian density function in QED for a free-fermion is:

$$\mathscr{L}_0 = \bar{\psi}(x)(i\gamma^\mu \partial_\mu - m)\psi(x) \tag{1.4}$$

where ψ is the Dirac field of mass m. Although 1.4 is already invariant for *global* U(1) transformation $\psi \to e^{-iqf}\psi$, it is not under *local* U(1) transformation (i.e. with a space-time dependent differentiable function f(x)):

$$\psi \to e^{-iqf(x)}\psi \tag{1.5}$$

Through the minimal substitution of the derivative with covariant derivative:

$$\partial_\mu \to D_\mu \equiv (\partial_\mu + iqA_\mu(x)) \tag{1.6}$$

where A_μ is the real electromagnetic field transforming as

$$A_\mu \to A_\mu \; - \frac{1}{q}\partial_\mu f(x) \tag{1.7}$$

the Lagrangian becomes invariant in the final form

$$\mathscr{L}_{QED} = \mathscr{L}_0 - q\bar{\psi}(x)\gamma^\mu \psi(x) A_\mu(x) - \frac{1}{4}F_{\mu\nu}F^{\mu\nu} \tag{1.8}$$

The second term in 1.8 represents the interaction between charged particles through the gauge field A_μ, i.e. the exchange of a photon. Local invariance also requires photon to be massless (otherwise, a term as $\frac{1}{2}mA_\mu A^\mu$ would emerge from the calculation), as experimentally verified. Finally, the masslessness of the photon also implies that electromagnetic interaction has infinite range.

Weak interaction

The first theory for weak processes was proposed by E. Fermi in 1934 [8]. In order to explain β-decay $n \rightarrow pe^{-}\bar{\nu}_e$, he introduced a current-current amplitude of the form:

$$\mathscr{M} = G_F(\bar{u}_p\gamma^{\mu}u_n)(\bar{u}_e\gamma_{\mu}u_{\nu_e}) \tag{1.9}$$

with the Fermi coupling constant $G_F/(\hbar c)^3 = 1.166 \cdot 10^{-5}$ GeV^{-2}. In 1957 C. S. Wu's experiment showed parity violation of ^{60}Co decay in ^{60}Ni that was not explained by Fermi's theory, therefore a new form of interaction was suggested by replacing γ^{μ} in Eq. 1.9 with $\gamma^{\mu}(1-\gamma^5)$. This is the so-called V-A structure of weak interactions that couples differently with left-handed and right-handed components of the spinors $\psi = \psi_L + \psi_R$ (i.e. the fermions).

In high energy approximation[1], leptonic currents involve only left-handed lepton fields. Limited to the case of leptonic interactions (i.e. for e, μ, τ and the corresponding neutrinos), for any Dirac spinor $\psi(x)$ we can define the weak *isospin* doublet:

$$\Psi_l^L(x) \equiv \begin{pmatrix} \psi_{\nu_l}^L(x) \\ \psi_l^L(x) \end{pmatrix} \tag{1.10}$$

with

$$\psi_{l,\nu_l}^L(x) = \frac{1}{2}(1-\gamma_5)\psi_{l,\nu_l}(x) \tag{1.11}$$

The formulation of weak interaction as gauge theory relies on the invariance under SU (2) local phase transformations:

$$\Psi_l^L(x) \rightarrow e^{ig\alpha_j(x)\tau_j/2}\Psi_l^L(x), \qquad \bar{\Psi}_l^L(x) \rightarrow \bar{\Psi}_l^L(x)e^{-ig\alpha_j(x)\tau_j/2} \tag{1.12}$$

---

[1] this weak theory is gauge-invariant only if leptons and bosons are considered massless. For high energy approximation we refer to E≫m.

where g is the weak coupling constant, τ_j are Pauli spin matrices and $\alpha_j(x)$ three arbitrary real differentiable functions of x. As it can be shown, we can obtain from this invariance three conserved weak currents:

$$J_j^\alpha(x) = \frac{1}{2}\bar{\Psi}_l^L(x)\gamma^\alpha\tau_j\Psi_l^L(x), \quad j = 1,2,3 \tag{1.13}$$

and finally the corresponding conserved charges, called *weak isospin charges*:

$$I_j^W = \int d^3x J_j^0(x), \quad j = 1,2,3 \tag{1.14}$$

The third current J_3^α is called *neutral* current, cause it couples also to electrically neutral leptons (i.e. neutrinos). As said above, we can define the *weak hypercharge* from the electric and weak charge:

$$\frac{Y}{2} = Q/e - I_3^W \tag{1.15}$$

so that left-handed ν_l has $I_3^W = \frac{1}{2}, Y = -1$ and the left-handed charged lepton has $I_3^W = -\frac{1}{2}, Y = -1$.

Flavor mixing: CKM matrix

Leptons form SU (2) doublets under the weak interaction:

$$\begin{pmatrix} \nu_e \\ e \end{pmatrix}, \quad \begin{pmatrix} \nu_\mu \\ \mu \end{pmatrix}, \quad \begin{pmatrix} \nu_\tau \\ \tau \end{pmatrix} \tag{1.16}$$

For quarks, the experimentally verified flavor change via W boson exchange must be taken into account, so that hadronic coupling is possible using the CKM rotation on quarks d, s, b. In this case, the flavor states are different from the mass states:

$$\begin{pmatrix} u \\ d' \end{pmatrix}, \quad \begin{pmatrix} c \\ s' \end{pmatrix}, \quad \begin{pmatrix} t \\ b' \end{pmatrix} \tag{1.17}$$

where the Cabibbo-Kobayashi-Maskawa (CKM) matrix (an unitary 3X3 matrix) operates on mass states d, s, b:

$$\begin{pmatrix} d' \\ s' \\ b' \end{pmatrix} = \begin{pmatrix} V_{ud} & V_{us} & V_{ub} \\ V_{cd} & V_{cs} & V_{cb} \\ V_{td} & V_{ts} & V_{tb} \end{pmatrix} \begin{pmatrix} d \\ s \\ b \end{pmatrix} \tag{1.18}$$

Electro-Weak Unification

In 1961, Glashow [9] proposed an unified gauge theory for QED and weak interactions, based on $\mathrm{SU}(2) \otimes U(1)$ group symmetry. Similar to QED, even weak lagrangian density can be made invariant under local gauge transformations (Eq. 1.12) through replacement of the derivative and the introduction of gauge fields. If we make both replacements valid for U(1) and SU (2) at same time:

$$\partial^\mu \to D^\mu = (\partial^\mu + ig\tau_j W_j^\mu(x)/2 - ig' B^\mu(x)/2) \tag{1.19}$$

where $\bar{W}^\mu$ is the real vector gauge field for weak interactions (according to SU (2) symmetry) and B^μ is the real gauge field for QED (according to U(1)), we obtain the invariant leptonic electro-weak Lagrangian density in the form $\mathcal{L}^L = \mathcal{L}_0 + \mathcal{L}_I$. In order to have a version of the function in the form

$$\mathcal{L}_I = \mathcal{L}_{CC} + \mathcal{L}_{NC} \tag{1.20}$$

where CC and NC indicate charged and neutral currents. It is usually used a linear combination of W_1^μ, W_2^μ for weak charged current while we write photon and Z^0 boson as linear combinations of B^μ and W_3^μ

$$W_\mu^{(\dagger)} = \frac{1}{\sqrt{2}}(W_{1\mu} \mp W_{2\mu}) \tag{1.21}$$

$$A_\mu = B_\mu \cos\theta_W + W_\mu^3 \sin\theta_W, \quad Z_\mu = -B_\mu \sin\theta_W + W_\mu^3 \sin\theta_W \tag{1.22}$$

$$g \sin\theta_W = g' \cos\theta_W = e \tag{1.23}$$

where θ_W is the Weinberg angle with a measured value of $\sin^2\theta_W = 0.2312 \pm 0.0006$ [4].

As we can see, from previuos formula it is straightforward to interpret the quanta of gauge fields as the EM and weak force mediators $\gamma, W^\pm, Z^0$.

So far, we have considered the fields as massless, as in Glashow's first theory, because of the gauge symmetry of the system. The Higgs mechanism was introduced to solve this problem adding the mass term for lepton and boson field, preserving at the same time gauge invariance.

1.1.3 Higgs mechanism: spontaneous symmetry breaking

The Higgs mechanims was proposed at the beginning of the '60s by several authors (Higgs, Englert, Guralnik *et al.*) [10, 11, 12] and has been fully incorporated into the SM by Weinberg and Salam [13, 14]. It relies on the idea to have a Lagrangian density invariant under a symmetry group of transformations that produces degenerate asymmetric states. Arbitrary selection of one of these states we have a *spontaneous symmetry breaking*. The core of the mechanism is to find a non-unique ground state (i.e. the *vacuum*) that implies a non-vanishing quantity in the system. This quantity will be assumed as the vacuum expectation value of quantized field.

In its simplest configuration the Higgs mechanism can be shown in a lagrangian density of scalar electrodynamics:

$$\mathscr{L}(x) = (D^{\mu}\varphi(x))^{*}(D_{\mu}\varphi(x)) - \mu^{2}\varphi^{*}(x)\varphi(x) - \lambda(\varphi^{*}(x)\varphi(x))^{2} - \frac{1}{4}F_{\mu\nu}(x)F^{\mu\nu}(x) \tag{1.24}$$

where D^{μ} is the covariant derivative 1.6 so that $\mathcal{L}$ is invariant under U(1) gauge transformations 1.5, λ and μ^2 are real parameters and $\varphi(x)$ is a complex scalar field that interact with the A_{μ} gauge field defined as usual by $F_{\mu\nu} = \partial_{\nu}A_{\mu} - \partial_{\mu}A_{\nu}$.

The potential part of the field $\mathscr{V}(\phi) = \mu^{2}\varphi^{*}(x)\varphi(x) + \lambda(\varphi^{*}(x)\varphi(x))^{2}$ depends on λ, μ^2 values. If we take $\lambda > 0$, two situations occour for the bounded potential: for $\mu^2 > 0$ $\mathscr{V}(\phi)$ has an absolute miminum at $\phi(x) = 0$, while for $\mu^2 < 0$ $\mathscr{V}(\phi)$ possesses a local minimum at $\phi(x) = 0$ and a whole circle of absolute minima, leading to a set of degenerate states i.e. different *vacuum states* (see fig. 1.1):

$$\phi(x) = \phi_0 = \left(\frac{-\mu^2}{2\lambda}\right)^{\frac{1}{2}} e^{i\theta}, \quad 0 \leq \theta < 2\pi \tag{1.25}$$

where the phase angle θ defines a direction in the complex ϕ-plane. Thanks to the invariance, gauge freedom allows to choose $\theta = 0$, leading to the *real* value $\phi_0 = \left(\frac{-\mu^2}{2\lambda}\right)^{\frac{1}{2}} \equiv \frac{1}{\sqrt{2}}\, v \ \ (> 0)$.

At the end, the original scalar field $\phi(x)$ can be expressed as a real field in a perturbative expansion of the chosen minimum:

$$\phi(x) = \frac{1}{\sqrt{2}}[v + \sigma(x)] \tag{1.26}$$

At this point we can say that symmetry of $\mathscr{V}(\phi)$ has been removed and ground states has *broken* the symmetry. Substituting 1.26 in 1.24 gives a form like $\mathcal{L}(x) = \mathcal{L}_0(x) + \mathcal{L}_I(x)$:

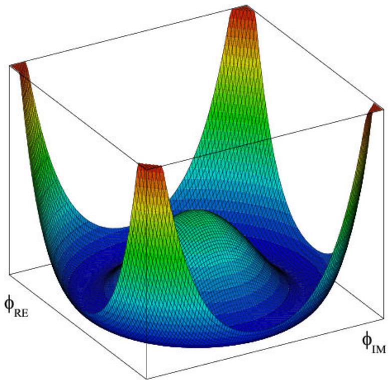

Figure 1.1 – Symmetry breaking for a complex scalar field $\phi(x) = 1/\sqrt{2}[\phi_1(x) + i\phi_2(x)]$ choosing $\mu^2 > 0$ in $\mathscr{V}(\phi)$

$$\begin{aligned}\mathcal{L}(x) \quad = \quad & \frac{1}{2}(\partial_\mu\sigma(x))(\partial^\mu\sigma(x)) - \frac{1}{2}(2\lambda v^2)\sigma^2(x) \\ & -\frac{1}{4}F_{\mu\nu}(x)F^{\mu\nu}(x) + \frac{1}{2}(qv^2)A_\mu(x)A^\mu(x) \\ & -\lambda v\sigma^3(x) - \frac{1}{4}\lambda\sigma^4(x) \\ & +\frac{1}{2}q^2A_\mu(x)A^\mu(x)[2v\sigma(x) + \sigma^2(x)] \qquad (1.27)\end{aligned}$$

The interpretation of the 1.27 terms brings to some crucial considerations. First two lines are $\mathcal{L}_0$, where we have a free scalar field $\sigma(x)$ with a mass $M_H = \sqrt{2\lambda v^2}$ and a *massive* vector field $A_\mu(x)$ of mass $|qv|$ replacing the initial massless gauge field. Second two lines represents the $\mathcal{L}_I$, with self-interaction of the scalar field and the interaction with the vector field with coupling strengths of q^2v and $\frac{1}{2}q^2$.

What we got is just the *spontaneous symmetry breaking* coming from the assignment of one initial degree of freedom of ϕ to the vector field A_μ, which then acquires mass. The massive spin 0 boson associated with the field $\sigma(x)$ is called *Higgs boson*.

Symmetry breaking in SM

Since electro-weak theory is $\mathrm{SU}(2) \otimes U(1)$ gauge invariant, the Higgs mechanism must be adapted to such a symmetry group in order to produce the lepton and boson masses and finally arrive to the Weinberg and Salam formulation [13]. In the following a brief description of the procedure is given. The basic idea is to introduce again an *Higgs field* that can break U(1) as well as SU (2) symmetry, so we use a weak isospin doublet made by two scalar fields:

$$\Phi(x) = \begin{pmatrix} \phi_a(x) \\ \phi_b(x) \end{pmatrix} \tag{1.28}$$

The 1.28 transforms in the same way that 1.10 under $\mathrm{SU}(2) \otimes U(1)$ gauge transformations. Including the Higgs field and its interactions with boson and lepton fields in the electro-weak Lagrangian, we obtain a generalized form as:

$$\mathcal{L} = \mathcal{L}^L + \mathcal{L}^B + \mathcal{L}^H + \mathcal{L}^{HL} \tag{1.29}$$

Next steps follows Higgs model searching for the vacuum state energy. The particular value:

$$\Phi_0 = \begin{pmatrix} \phi_a^0 \\ \phi_b^0 \end{pmatrix} = \begin{pmatrix} 0 \\ v/\sqrt{2} \end{pmatrix} \tag{1.30}$$

where $v = (-\mu^2/\lambda)^{1/2}$, is chosen for the ground state, so that we derive the Higgs field as $\Phi(x) = \frac{1}{\sqrt{2}}\binom{0}{v+\sigma(x)}$, as in 1.26. Since the process began with a doublet of complex scalar fields and finished with a real doublet, we can say that in the Lagrangian three degrees of freedom are absorbed by the $W^{\pm}, Z$ bosons to aquire mass, while the photon remain massless as desired and the scalar massive Higgs boson comes from $\sigma(x)$, with a mass $M_H = \sqrt{2\lambda v^2}$ that is a free parameter to be measured experimentally.

Lepton and quark masses arise from Yukawa interactions with the scalar Higgs. They are directly proportional to Yukawa coupling constants $Y_{q,l}$ and are expressed, in lepton case, in $\mathcal{L}^{LH}$ part:

$$\begin{aligned}\mathcal{L}^{LH}(x) &= -Y_l[\bar{\Psi}_l^L(x)\psi_l^R(x)\Phi(x) + \Phi^\dagger\bar{\psi}_l^R(x)\Psi_l^L(x)] \\ &\quad -Y_{\nu_l}[\bar{\Psi}_l^L(x)\psi_{\nu_l}^R(x)\tilde{\Phi}(x) + \tilde{\Phi}^\dagger\bar{\psi}_{\nu_l}^R(x)\Psi_l^L(x)] \qquad (1.31)\end{aligned}$$

where $\tilde{\Phi}(x) = -i[\Phi^\dagger(x)\tau_2]^T$. The masses are introducted as parameters to be experimentally measured, derived from coupling constants and the Higgs field:

$$m_l = Y_l\frac{v}{\sqrt{2}} \qquad (1.32)$$

In quarks case, we must take in account that also upper member of quark doublet must have mass. To acquire this feature the Higgs doublet is reconstructed as $\Phi_c = -i\tau_2\Phi^*(x)$ and an hermitian conjugate member is added to the lagrangian. Since the vacuum expectation value of the Higgs field is $v = 246$ GeV, the Top quark Yukawa coupling is:

$$Y_t = \frac{m_{\text{top}}\sqrt{2}}{v} \sim 1 \qquad (1.33)$$

1.2 Searching for a new particle

The classic particle physics experiment is the search for something new or unexpected. For a fundamental particle to have escaped detection thus far, it must either be difficult to produce in an accelerator, difficult to detect, or both. Particles can be difficult to produce if they have a small coupling to normal matter or if their mass is near the upper limit of the accelerator's reach. Detection is difficult for particles with small couplings, but their presence can still be inferred from the energy and momentum they carry away from an interaction, as is done for neutrinos. Detection is also difficult if particles are massive and quickly decay into ordinary quarks and leptons. Only by reconstructing all the outgoing secondary decay products in a large set of collisions (or events) can the parent particle be inferred. For masses well above the top quark, decay to any allowed combination of fermions is energetically possible, complicating the types of detector signal one must include in the search. Identifying a few unusual events in a sea of trillions of ordinary processes is the challenge which must be overcome to discover new phenomena.

As mentioned earlier, much of the evolution of particle physics has been based on the discovery of new patterns and symmetries. Most theoretical predictions for modifying or extending the Standard Model are based on plausible new symmetries which include additional particles. We begin our search for novel features in the data by narrowing our focus using some general assumptions about the new physics considered. We are interested in the generic case that some Standard Model particles are mirrored at higher mass-scales, remaining undiscovered; this is analogous to the way the second and third generation particles are identical to the first generation but with larger masses. High precision measurements of the Z width at LEP and SLC have excluded with great confidence the existence of a fourth generation neutrino of small mass. Similarly, searches for fourth generation quarks have proven unsuccessful.

The CDF collaboration reached the conclusion that there is still an opportunity to further the search for massive new electroweak bosons, denoted W' and Z'. In particular, CDF has expertise and analysis tools suited to the study of decays involving top quarks. The CDF collaboration has recently completed a search for $Z' \to t\bar{t}$ [21], that is so far the most sensitive search for $t\bar{t}$ resonances below 1 TeV. The most recent analyses from Tevatron/LHC experiments have already excluded a benchmark leptophobic Z' model below 1 TeV. But CDF is still more sensitive to models with a lower cross-section and/or lower branching ratios. The cross-section for SM $t\bar{t}$ production at LHC is almost twenty times higher than at the Tevatron; as a result, LHC analyses are affected by a larger background due to $t\bar{t}$ production. Even though for medium Z' masses the cross-section is five times higher at LHC [22], CDF is still two times more sensitive for a boson with mass below 800 TeV. Figure 1.2 shows a comparison of the expected limits from CMS and from the most recent CDF analysis with the full dataset: only CDF is sensitive to possible narrow resonances with a cross-section 10 times lower than benchmark Z' model in the low mass region.

The CDF Z' analysis was performed selecting events with at least four jets and a lepton in the final state. In this way was isolated a sample composed primarily by $t\bar{t}$ events where the top-antitop pair decays in two W bosons and two b-quarks and one W decays leptonically and the other one hadronically. The profile of the invariant mass of all the reconstructed objects and missing transverse energy was used as a final discriminant between Z' signal and backgrounds. In Table 1.2 the results with the expected and observed limits are shown.

Preliminary studies indicate that CDF has a better sensitivity than the LHC also for a W' with mass just above the tb mass, giving the opportunity to

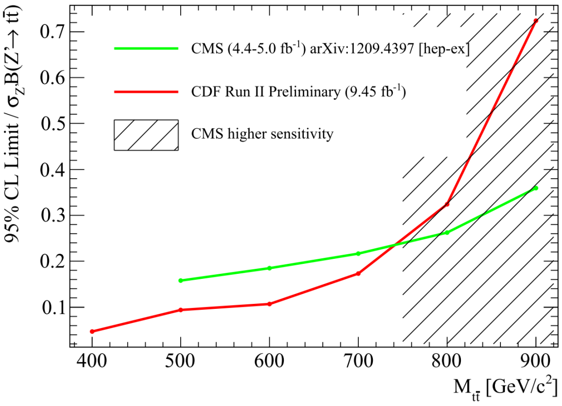

Figure 1.2 – Comparison plot between observed limits for CDF (red) and CMS (green). On the x-axis: value of $M_{Z'}$; on the y-axis: 95% CL observed limit normalized to the theoretical cross-section to compare the results of Tevatron and LHC.

perform a study that is complementary to the $Z' \rightarrow t\bar{t}$ one. As for the Z' analysis, Tevatron and LHC experiments have already looked for a W', excluding a benchmark W' model below 2 TeV. In particular, in 2009 CDF set limits for W' production searching for a boson in events with a top and a bottom quark, where the top decays in a W boson and a bottom quark and the W decays leptonically. The invariant mass of the lepton, the neutrino and the two b-jets in the final state was used to discriminate W' events from the background. In Table 1.3 the expected and observed limits from the 2009 analysis are shown. Figure 1.3 shows a comparison of the expected limits on W' production from the most recent Tevatron/LHC analyses.

The object of this thesis is updating the W' analysis with the full CDF dataset collected to the end of the Tevatron run in September 2011, corresponding to an integrated luminosity of 10 fb^{-1}. In particular, we look for W' in events where the lepton that comes from the W decay is not reconstructed or is a τ that decays hadronically, relying solely on the signature of high p_T jets and large missing transverse energy. Results from the analysis in the missing transverse energy plus jets sample can be combined with lepton

$M_{Z'}$ (GeV/c^2)	Expected (pb)	Observed (pb)
350	0.772	0.687
400	0.575	0.652
450	0.670	0.585
500	0.520	0.427
550	0.354	0.530
600	0.245	0.472
650	0.199	0.269
700	0.159	0.145
750	0.137	0.112
800	0.115	0.099
850	0.106	0.103
900	0.097	0.116
950	0.091	0.118
1000	0.092	0.129
1100	0.098	0.132
1200	0.134	0.166

Table 1.2 – CDF 95% CL expected and observed limit for Z' mass points as a function of Z' mass. From [21].

$M_{W'}$ (GeV/c^2)	Expected (pb)	Observed (pb)
300	1.56	1.59
400	1.04	1.17
500	0.74	0.84
600	0.54	0.44
650	0.46	0.39
700	0.40	0.32
750	0.33	0.28
800	0.30	0.26
850	0.28	0.25
900	0.28	0.26
950	0.30	0.28

Table 1.3 – CDF 95% CL expected and observed limit for W' mass points as a function of W' mass. From [19].

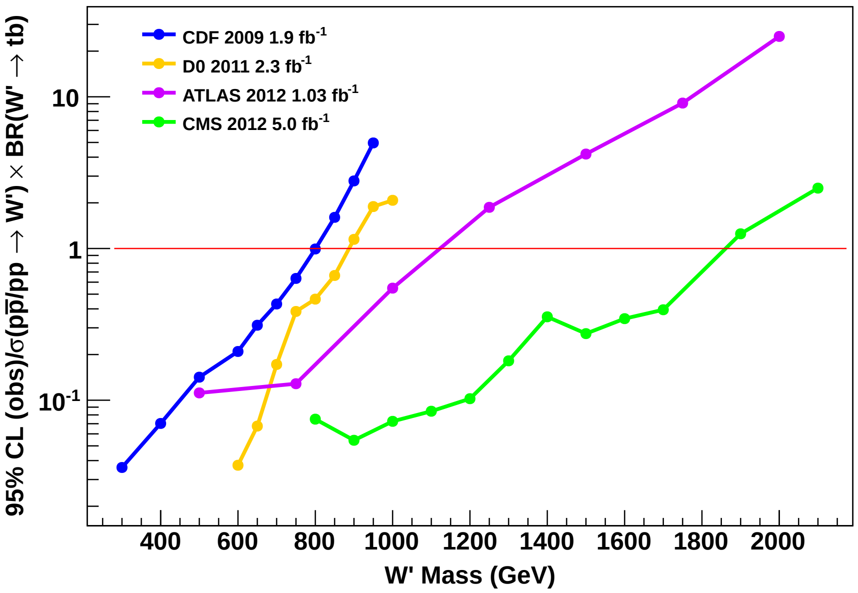

Figure 1.3 – Comparison plot between the four analyses considered in the comparative study. On the x-axis: value of $M_{W'}$; on the y-axis: 95% CL observed limit normalized to the theoretical cross-section to compare the results of Tevatron and LHC.

plus jets one, resulting in more stringent limits. Furthermore, the combined result is going to be a sensitivity benchmark for other more elusive new physics searches with the same final state, such as the search for charged Higgs production [23].

1.3 Features of a W'

A W'-like boson which decays via tb occurs in a variety of proposed BSM models: as the excitations of the W boson in Kaluza-Klein extra-dimension [15], as the techni-ρ of technicolor theories [16], or as a bosonic partner in Little Higgs scenarios [17]. The classic W' is a simple extension of the Standard Model to the left-right symmetric group $\mathrm{SU}(2)_L \times \mathrm{SU}_R(2) \times \mathrm{U}(1)$ [18], which has a right-handed charged boson W'_R with universal weak coupling strength and large mass. Searches in the tb can probe models where the couplings are unknown or where the leptonic channels are suppressed. The Lagrangian describing the W' coupling to fermions can be written as

$$\mathcal{L} = \frac{g}{\sqrt{2}} \bar{f}_i \gamma_\mu \left(a^L_{f_i f_j} P_L + a^R_{f_i f_j} P_R \right) W'^{\mu} f_j + \text{H.c.} \tag{1.34}$$

where $P_{L,R} = (1 \pm \gamma^5)/2$ are the projection operators, g is the gauge coupling, and the $a^{L,R}_{f_i f_j}$ are arbitrary couplings that may differ for quarks and leptons.

To restrict our search such as to make a quantitative measurement, some general assumptions must be made. Our signal model assumes a W' with unknown mass, unspecified coupling strength to tb, and purely right- or left-handed chirality (W'_R or W'_L); this is referred to as a SM-like W'.

The W' is produced entirely via an s-channel process; contributions from the t and u channels are suppressed by the large W' mass. Like the Standard Model W boson, the W' decays nearly instantaneously to a quark-antiquark pair, or to a lepton and a neutrino. This search is focused on the events that decay to tb, which occur about one fourth of the time. Our model assumes a narrow W' width, i.e. the width of the reconstructed resonance is determined by detector resolution rather than the intrinsic width. The interference between the W boson and W'_L is model-dependent and constrained to be very small, so this term is neglected in our signal model.

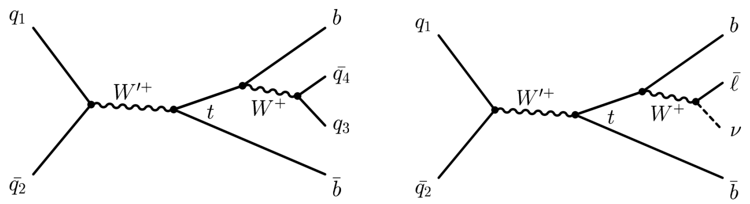

Figure 1.4 – Feynman diagram for W' s-channel production and subsequent hadronic (left) and leptonic (right) decay of the W originated from t.

Chapter 2

The Experiment

2.1 The Tevatron Collider

The Tevatron is a proton-antiproton accelerator located at the Fermi National Accelerator Laboratory (`FNAL`) and producing $p\bar{p}$ collisions at a center-of-mass energy of $\sqrt{s}$ = 1.96 TeV. Proton and antiprotons collide at two interaction points, where the Collider Detector at Fermilab (`CDF`) and `DØ` detectors are installed. The Tevatron proton and antiproton beams are produced by a chain of accelerators, which take care of proton and antiproton production, antiproton storage, and intermediate acceleration up to the injection into the Tevatron ring. The Tevatron acceleration complex is shown in Fig. 2.1.

2.1.1 The Proton Source

The acceleration cycle of the proton beam begins with the production of negatively ionized hydrogen atoms, H^- [1] , which are initially accelerated to a kinetic energy of 750 KeV by a Cockroft-Walton electrostatic accelerator. Preaccelerated H^- ions are then injected into the LINAC, where they

---

[1] At sub-relativistic energies one must accelerate negative ions rather than positive protons in order to avoid heavy beam neutralization and loss by electron capture.

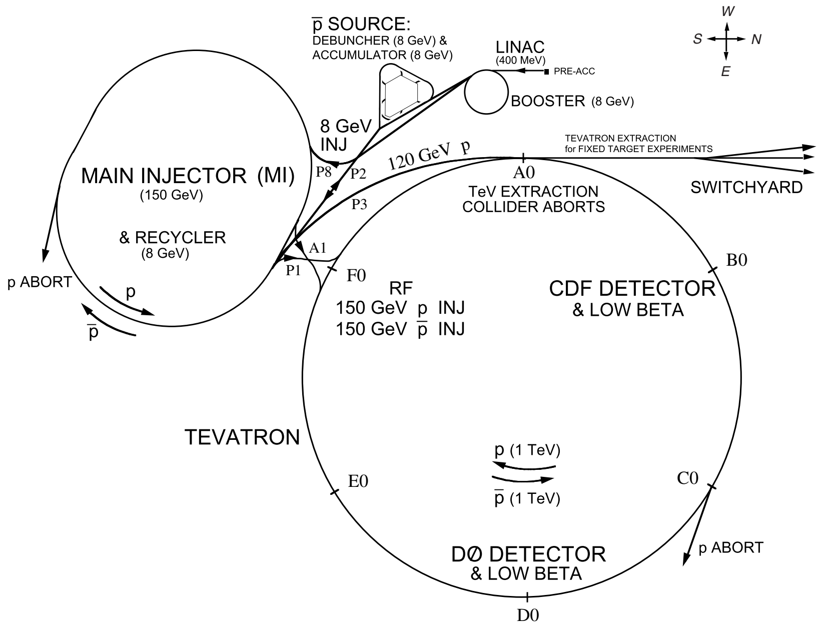

Figure 2.1 – The Fermilab accelerator system and the Tevatron collider.

reach an energy of 400 MeV by traveling through a 150 m long chain of radio-frequency (RF) accelerating cavities. Prior to being injected into the *Booster*, the H^- ions pass through a carbon foil which strips their electrons off. In the booster the protons are accelerated to 8 GeV by a number of RF cavities and then they are transferred to another synchrotron, called *Main Injector*[2], which brings their energy up to 150 GeV. This is the final step before protons are injected into the Tevatron.

2.1.2 The Antiproton Source

The production of the antiproton beam is significantly more complicated. The cycle starts with the extraction from the Main Injector of a 120 GeV proton beam, which is directed onto a Nickel alloy target. The collisions creates a variety of different particles, among which are $\bar{p}$, that are produced with an efficiency of about 18 $\bar{p}/10^6$ p. The particles, coming off the

---

[2] Completed in 1999 for Run II, it is located in a 3 km circumference tunnel which houses also the antiproton Recycler and is approximately tangent to the Tevatron.

target at different angles, are focused into a beam line by means of a magnetic lithium collection lens. In order to select only the antiprotons, the beam is sent through a pulsed magnet which acts as a charge-mass spectrometer. The emerging antiprotons, which have a bunch structure similar to that of the incident protons and a large momentum spread, are stored in the *Debuncher*, a storage ring where the $\bar{p}$ momentum spread is reduced via stochastic cooling [3].

At the end of the debunching process the bunch structure is destroyed, resulting in a continuous beam of 8 GeV antiprotons which are successively transferred to the *Accumulator*. The Accumulator is a triangle-shaped storage ring, housed in the same tunnel as the Debuncher, where the antiprotons are further cooled down and stored until all the Debuncher cycles are completed. When the collected antiprotons saturate the Accumulator acceptance ($\sim 6\times10^{11}$ antiprotons), they are transferred to the *Recycler* [4], a 8 GeV fixed energy storage ring with a larger acceptance, made of permanent magnets and placed in the Main Injector enclosure. In the Recycler the size and spread of the antiproton beam is further shrunk by the electron cooling process: in a straight section of the Recycler a beam of electrons travels close to the antiprotons at the same velocity, absorbing energy from the antiprotons. When a current sufficient to create 36 bunches with the required density is available, the $\bar{p}$ are injected into the Main Injector where they are accelerated to 150 GeV. At this point also the antiprotons are ready to be injected into the Tevatron, in opposite direction to the proton beam.

---

[3] Stochastic cooling is a technique used to reduce the transverse momentum and energy spread of a particle beam without any accompanying beam-loss. This is achieved by iteratively applying a feedback mechanism that senses the beam deviation from the ideal orbit with a set of electrostatic plates, processes and amplifies the signal, and transmits an adequately-sized synchronized correction pulse to another set of plates downstream.

[4] Antiproton availability is the most limiting factor at the Tevatron for attaining high luminosities: keeping a large antiproton beam inside the Recycler has been one of the most significant engineering challenges and the excellent performance of the Recycler has been an achievement of prime importance for the good operation of the accelerator.

2.1.3 The Tevatron Ring

The Tevatron is a 1 km-radius superconducting synchrotron that accelerates particles from 150 GeV to 980 GeV. The proton and antiproton beams circulate in opposite directions in the same beam pipe. Electrostatic separators produce a strong electric field that keeps the two beams away from each other except at the collision points. The beam is steered by 77 superconducting dipole magnets with a maximum magnetic field of 4.2 T and focused by 240 quadrupole magnets. A cryogenic system based on a liquid nitrogen followed by a liquid helium state cools down the Tevatron magnets to 4.2 K, at which temperature the niobium-titanium alloy of the magnet coils becomes superconducting. The process of injecting particles into the machine, accelerating them, and initiating collisions is referred to as a *shot*. It starts with the injection from the Main Injector of 150 GeV protons, two bunches at a time. Once the proton beam is in the machine, groups of four antiprotons bunches are mined from the Recycler, accelerated to 150 GeV in the Main Injector and injected into the Tevatron. The RF cavities accelerate the beams to 980 GeV, electrostatic separators switch polarity and cause the beams to collide at two points. Each interaction point lies at the center of a particle detector: DØ named after its location in the Tevatron optics, and CDF, located at BØ.
Successively, beams are scraped with remotely-operated collimators to remove the beam halo and, as soon as the beam conditions are stable, the experiments begin to take data. A continuous period of collider operation with the same proton and antiproton beams is called a *store*.

2.1.4 Luminosity and Tevatron Performance

The performance of a collider is evaluated in terms of two key parameters: the available center-of-mass energy, $\sqrt{s}$, and the instantaneous luminosity, $\mathcal{L}$. The former defines the accessible phase-space for the production of final

Parameter	Run II value
number of bunches (N_b)	36
revolution frequency [MHz] (f)	1.7
bunch rms [m] σ_l	0.37
bunch spacing [ns]	396
protons/bunch (N_p)	2.7×10^{11}
antiprotons/bunch ($N_{\bar{p}}$)	3.0×10^{10}
total antiprotons	1.1×10^{12}
β^* [cm]	35

Table 2.1 – Accelerator nominal parameters for Run II configuration.

state particles. The latter is defined as the interaction rate per unit cross section of the colliding beams (collisions/(cm^2·s)). In the absence of a crossing angle or position offset of the beams, the luminosity at CDF or DØ, is given by the expression:

$$\mathcal{L} = \frac{f N_b N_p N_{\bar{p}}}{2\pi(\sigma_p^2 + \sigma_{\bar{p}}^2)} F\left(\frac{\sigma_l}{\beta^*}\right), \tag{2.1}$$

where f is the revolution frequency, N_b is the number of bunches, $N_{p(\bar{p})}$ is the number of protons (antiprotons) per bunch, and $\sigma_{p(\bar{p})}$ is the transverse proton (antiproton) beam size at the interaction point. F is a form factor with a complicated dependence on the beta function value at the interaction point, β^* [5], and the bunch length, σ_l.

Tab. 2.1 shows the design Run II accelerator parameters, while Fig. 2.2 shows the evolution of the integrated luminosity, defined as $L = \int \mathcal{L} dt$, and the instantaneous luminosity at the start of Tevatron stores during the Run II. The steady increase of the integrated luminosity and the continuous improvement of the instantaneous luminosity prove the outstanding performance of the accelerator.

The Tevatron program was terminated on September 30, 2011. During the Run II the Tevatron delivered 12 fb^{-1} of data per experiment, $\sim$ 10 of which were collected by the CDF and DØ detectors.

---

[5] The suitably normalized *beta function* (β^*) represents a measure of the local transverse beam size.

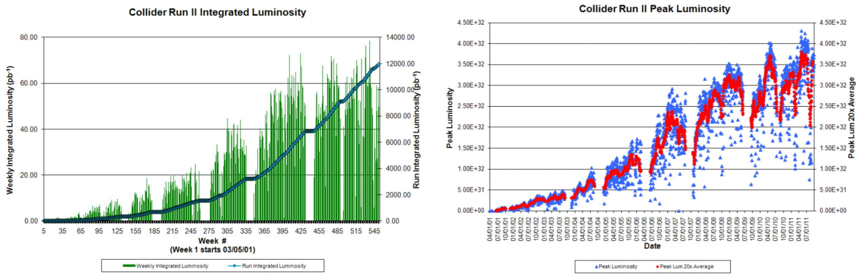

Figure 2.2 – Tevatron integrated luminosity as a function of Run II weeks (left) and peak luminosity as a function of calendar date (right). Empty regions correspond to Tevatron shut-down periods.

2.2 The CDF II detector

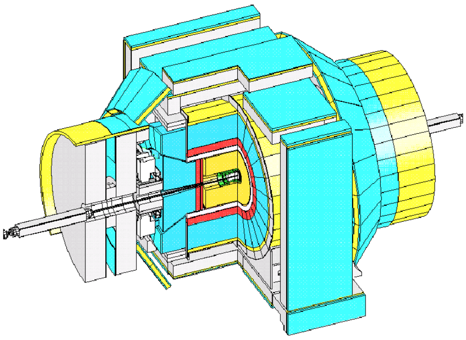

Figure 2.3 – Isometric view of the CDF II Detector.

The CDF II detector is an azimuthally and forward-backward symmetric apparatus designed to study the $p\bar{p}$ collisions at the BØ interaction point of the Tevatron. A detailed description of the CDF II detector is given in ref fixme. However, in order to make this document self-consistent, simplified information on the complete detector is also given in the following.

CDF II is a general purpose, cylindrical-shaped detector (Fig. 2.3), which in the Run II configuration comprises:

- a **tracking system**, which comprises three silicon microstrip trackers (L00, SVX and ISL) and an open-cell drift chamber (COT) inside a superconducting solenoid, that provides a constant 1.4 T magnetic field parallel to the beam direction, with the purpose of bending into helixes the trajectories of charge particles to allow determining their momentum and charge;

- a **Time of Flight** system (TOF), located outside the `COT`, for measuring the mass of charged particles with momenta up to 2 GeV/c;
- a **calorimeter system**, with the purpose of measuring the energy of charged and neutral particles[6];
- **muon chambers and scintillators**, used to track and identify muons, that pass through the calorimeters interacting as minimum ionizing particles (m.i.p.);
- **luminosity monitors**, for the instantaneous luminosity measurement, necessary to derive cross section from event yields.

2.2.1 Coordinates system and standard definitions at CDF

`CDF` adopts a left-handed Cartesian coordinate system with origin at the nominal BØ interaction point, coincident with the center of the drift chamber. The positive z-axis lies along the nominal beam-line and has the direction of the proton beam (eastward). The x-y plane is therefore perpendicular to the beam-line, with the y-axis pointing upwards and the x-axis in the horizontal plane, pointing radially outward with respect the center of the accelerator ring. A cylindrical (r, ϕ, z) coordinate system is particularly convenient to describe the detector geometry, where

$$r = \sqrt{x^2 + y^2} \quad \text{and} \quad \phi = \tan^{-1} \frac{y}{x} \,. \tag{2.2}$$

A momentum-dependent particle coordinate, named *rapidity*, is also commonly used in high-energy physics for its transformation properties under

---

[6] The muons, whose momentum is measured in the tracker, are an exception.

Lorentz boosts. The rapidity is defined as

$$Y = \frac{1}{2} \ln \frac{E + p_z}{E - p_z} , \tag{2.3}$$

where E is the energy and p_z is the z component of the particle momentum. Rapidity intervals turn out to be Lorentz invariant. In the relativistic limit, or when the mass of the particle is negligible, rapidity depends only upon the production angle of the particle with respect to the beam axis, $\theta = \tan^{-1} \frac{\sqrt{x^2+y^2}}{z}$. This approximation is called *pseudorapidity* η and is defined as

$$Y \overset{p \gg m}{\rightarrow} \eta = -\ln \left(\tan \frac{\theta}{2} \right) . \tag{2.4}$$

A value of $\theta = 90^\circ$, perpendicular to the beam axis, corresponds to $\eta = 0$. Since the event-by-event longitudinal position of the interaction is distributed around the nominal interaction point with a 30 cm RMS width, sometimes a distinction between the detector pseudorapidity (usually indicated with η_{det}), measured with respect to the $(0, 0, 0)$ nominal interaction point, and the event pseudorapidity (η), which is measured with respect to the z position of the actual event vertex, is considered.

The spatial separation between particles in the detector is commonly given in terms of a Lorentz invariant variable defined as:

$$\Delta R = \sqrt{\Delta\phi^2 + \Delta\eta^2}. \tag{2.5}$$

Other quantities useful to describe the kinematics of $p\bar{p}$ interactions are the transverse momentum and the transverse energy, defined as $p_T = p \sin\theta$ and $E_T = E \sin\theta$, respectively.

2.3 The tracking system

A three-dimensional tracking of charged particles is achieved through an integrated system consisting of three inner silicon subdetectors and a large outer drift-chamber, all immersed in the magnetic field of the superconducting solenoid. The silicon detectors provide a precise determination of the track impact parameter, the azimuthal angle and the z coordinate at production, whereas the drift chamber has excellent resolution on the transverse momentum, ϕ and η. The combined information of the tracking detectors provides very accurate measurements of the helical paths of charged particles inside the detector. We will describe this system starting from the devices closest to the beam and moving outwards (see Fig. 2.4).

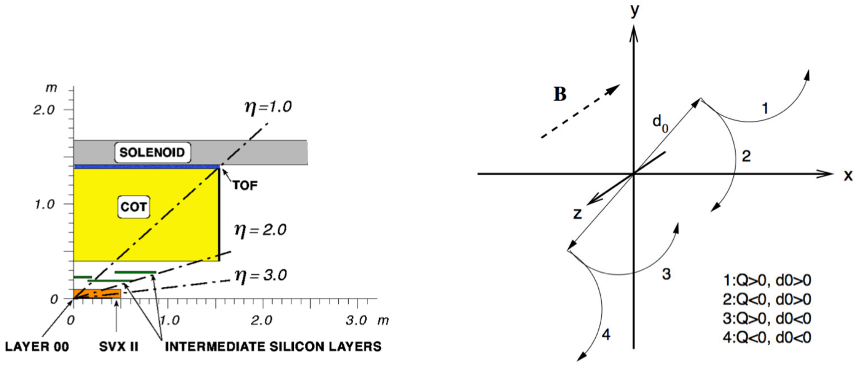

Figure 2.4 – (left) The CDF II tracker layout showing the different subdetector systems. (right) Schematic drawing of the impact parameter d_0. The sign of the impact parameter is defined as positive or negative with reference to the direction of the track momentum vector (in the X,Y quadrant in the drawing).

2.3.1 The Silicon Tracker

The full CDF silicon detector is composed of three approximately cylindrical coaxial subsystems: the Layer 00 (L00), the *Silicon Vertex* detector (SVX) and the Intermediate *Silicon Layers* (ISL).

Silicon sensors operate as reverse-biased *p-n* junctions. By segmenting the *p* or *n* side of the junctions into *strips* and reading out the charge deposition separately on every strip the point of trasversal of a charged particle is measured. At `CDF` the typical distance between two strips is about 60 μm. There are two types of microstrip detectors: single- and double-sided. In single-sided detectors only the p-side of the junction is segmented into strips, while double-sided detectors have both sides of the junction segmented into strips. Single-sided sensors have strips parallel to the z direction and provide only r-ϕ position measurements, while double-sided detectors have strips at an angle (stereo angle) with respect to the z direction on one side and, therefore, provide also information on the particle position along z.

L00 is a 90 cm-long, radiation hard, assembly of single-sided silicon detectors, structured in longitudinal strips. The detector tiles are mounted directly on the beam pipe at 1.35-1.62 cm from the beam axis. The detector support structure is in carbon fiber with integrated cooling system. Being so close to the beam, `L00` allows to reach a resolution of $\sim$ 25–30 μm on the impact parameter of tracks of moderate p_T , providing a powerful handle to identify long-lived hadrons containing a b quark.

SVX is composed of three 29 cm-long cylindrical barrels, radially organized in five layers of double-sided silicon wafers extending from 2.5 cm to 10.7 mm (see Fig. 2.5). Each barrel is segmented into 12 wedges, each covering $\sim 30^\circ$ in ϕ. The double-side structure of the wafers allows a three dimensional position measurement: one side of the wafer has axial strips (parallel to the beam), the other one has either 90° strips (perpendicular to the beam) or 1.2° stereo strips (at small angle with respect to the beam). This detector provides position information with a 12 μm resolution on the single hit and some dE/dx ionization information.

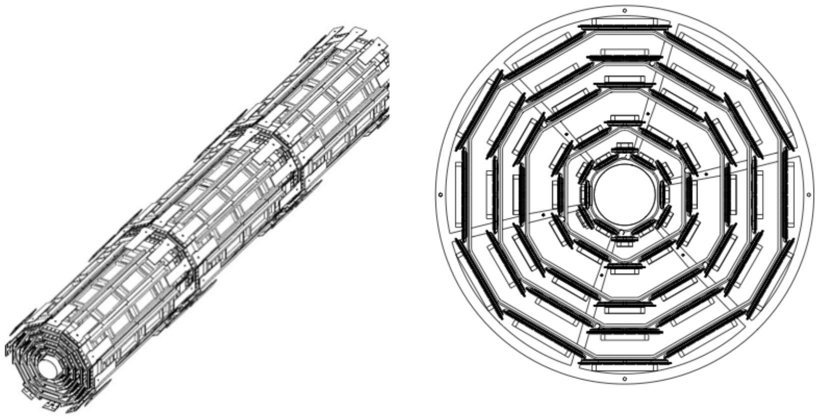

Figure 2.5 – The SVX silicon detector: on the left, a three-dimensional view of the detector allows to see the barrel structure along the beam axes; on the right, the transverse plane section shows in detail the layer sequence.

ISL consists of two layers of double sided silicon wafers, similar to those of SVX, one of which is assembled in a twofold telescopes with planes at a radial distance of 22 cm and 29 cm from the beam-line and covering $1 < |\eta| < 2$. One single central layer is located at r = 22 cm, covering $|\eta| < 1$. The two ISL layers are important to increase the tracking coverage in the forward region, where the COT coverage is limited, and to improve the matching between SVX and COT tracks.

The combined resolution of the CDF inner trackers for high momentum tracks is ~ 40 μm in impact parameter and ~ 70 μm along the z direction. All silicon detectors are used in the off-line track reconstruction algorithms, while SVX plays a crucial role also in the on-line track reconstruction of the trigger system. The CDF trigger employs an innovative processor, the Silicon Vertex Trigger (SVT) [27, 28], which uses the SVX information to measure the track impact parameter on-line with a resolution of < 20 μm, that allows to resolve the secondary vertices, displaced from the primary interaction point, such as those produced in B hadron decays.

2.3.2 Central Outer Tracker

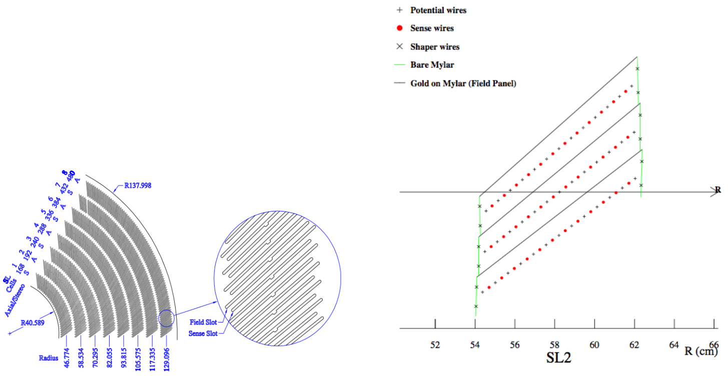

Figure 2.6 – Left: 60° section of the COT end-plate (left). For each super-layer the total number of cells, the wire orientation (axial or stereo) and the average radius in cm are shown. The enlargement shows in detail the slot where the wire planes (sense and field) are installed. Right: cross-section of three axial cells in super-layer 2; the arrow indicates the radial direction.

Surrounding the silicon detector is the Central Outer Tracker (COT) [29]. It is a 3.1 m-long cylindrical drift chamber, coaxial with the beam, which covers the radial range from 40 to 137 cm for $|\eta| < 1$. The COT contains 96 sense wire layers, which are radially grouped into 8 superlayers, as inferred from the end plate slot structure shown in Fig. 2.6. Each superlayer is divided in ϕ into supercells, and each supercell has 12 alternated sense and field-shaping wires. The maximum drift distance is approximately the same for all superlayers. Therefore, the number of supercells in a given superlayer scales approximately with the radius of the superlayer. The entire COT contains 30240 sense wires. Approximately half the wires run along the z direction (*axial* wires), the other half are strung at a small stereo angles (2°) with respect to the z direction (*stereo* wires). The combination of the axial and stereo information allows to measure the z positions and a three-dimensional reconstruction of tracks. Particles originated from the interaction point, which have $|\eta| < 1$, pass through all the 8 COT superlayers. The COT is filled with an argon-ethane gas mixture and isopropyl alcohol (49.5:49.5:1). The mixture is chosen in order to have a constant drift velocity, approximately 50 μm/ns, across the cell width. The maximum electron drift time is approximately 100 ns. Due to the magnetic field that the COT is immersed in, electrons drift at a Lorentz angle of 35°. The supercells are tilted by 35° with respect to the radial direction to compensate for this effect and make the drift path perpendicular to the radial direction.

The hit position resolution in the r-ϕ plane is about 140 μm. Tracking algorithms are utilized to reconstruct particle trajectories (helices) that best-fit to the observed hits. The reconstructed trajectories are referred to as *tracks*. Particle momentum and charge are determined from the bending of tracks in the magnetic field. The COT hits are also processed on-line by the XFT, which reconstructs the tracks used in LEVEL 1 of the trigger system, (Sec. 2.7.4). The transverse momentum resolution of off-line tracks, measured using cosmic ray events, is

$$\frac{\sigma_{p_T}}{p_T^2} = 0.017\ (\mathrm{GeV}/c)^{-1} \tag{2.6}$$

for tracks with $p_T > 2$ GeV/c [31].

2.3.3 Time Of Flight

The CDF II Time of Flight (TOF) detector lies just outside the tracking system, supported on the inner wall of the solenoid (Fig. 2.4). It is a barrel of 3 m long scintillators bars located at 140 cm from the beam line with a total of 216 bars, each covering 1.7° in φ and the pseudorapidity range $|\eta| < 1$. Light is collected by photomultipliers at both ends of the bar. Single hit position in the TOF is determined by the comparison of the signal times of the photomultipliers. Particle identification is achieved by measuring the time of arrival of a charged particle at the scintillators with respect to the collision time. Thus, combining the measured time-of-flight T, the momentum and the path length the mass of the particle can be estimated.

$$m = \frac{p}{c}\sqrt{\frac{1}{\beta^2} - 1} = \frac{p}{c}\sqrt{(\frac{cT}{L})^2 - 1} \tag{2.7}$$

where the momentum p and the path length L are precisely measured by the tracking system. For the TOF measurement the collision time must be known and this is found with a 50 ps uncertainty by a best-fit process over all tracks in the event. The design resolution in the time-of-flight measurement is $\approx$ 120 ps and provides at least two standard deviation separation between $K^\pm$ and $\pi^\pm$ for momenta $p < 1.6$ GeV/c.

2.4 Calorimeter

The calorimeter system, together with the muon and tracking systems, represents one of the main sub-detector of CDF II. A detailed description of this system can be found in the CDF Technical Design Report [32].

The CDF calorimetry system has been designed to measure energy and direction of neutral and charged particles leaving the tracking region. In particular, it is devoted to jet reconstruction and it is also used to measure the missing energy associated to neutrinos. Particles hitting the calorimeter can be divided in two classes, according to their main interaction with matter: electromagnetically interacting particles, such as electrons and photons, and hadronically interacting particles, such as mesons or barions produced in hadronization processes. To detect these two classes of particles, two different calorimetric parts have been developed: an inner electromagnetic and an outer hadronic section, providing coverage up to $|\eta| < 3.64$.

In order to supply information on particle position, the calorimeter is also segmented in towers, projected toward the geometrical center of the detector. Each tower consists of alternating layers of passive material and scintillator tiles. The signal is read out via wavelength shifters (WLS) em-

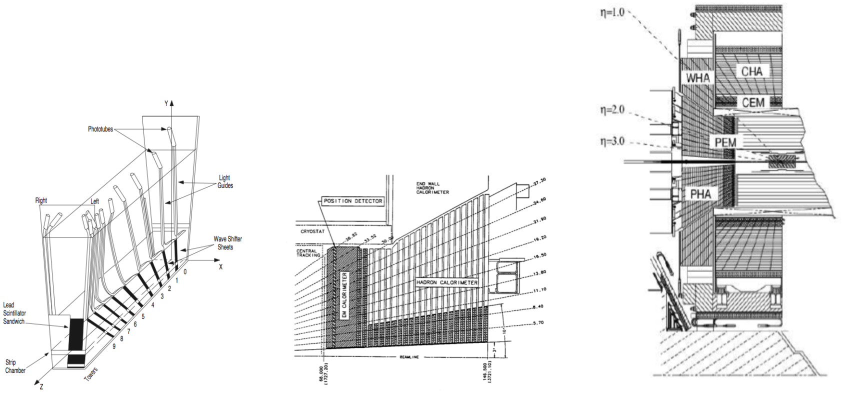

Figure 2.7 – (left) artist view of a central calorimeter wedge showing the pipes collecting light from the front electromagnetic towers; (center) cut view of the plug; (right) elevation view of the detector showing the components of the calorimeter system.

bedded in the scintillator and light from WLS is then carried by light guides to photomultiplier tubes. The central sector of the calorimeter, covering the region $|\eta| < 1.1$, was recycled from Run I, while brand new calorimeters (called plug calorimeters) were built up to cover the forward and backward regions. Figure 2.7 shows the main components of the calorimeter system.

2.4.1 The Central Calorimeter

Excluding upgrades on the readout electronics, needed to cope with the increased collision rate, the central calorimeter is the same as in Run I[7]. The Central Electro-Magnetic calorimeter (`CEM`) is segmented in $\Delta\eta \times \Delta\phi = 0.11 \times 15^\circ$ projective towers consisting of 31 alternate layers of lead and scintillator, for a total material depth of 19 X_0 [8]. The Central and End-

---

[7] `CDF`, from 1992 to 2004, used embedded layers of gas proportional chambers in the central calorimeter to improve the identification of electrons and photons (*Central Preshower* (CPR) and *Central Crack* (CCR) detectors). Late in 2004 the `CDF` Central Preshower and Crack Detector Upgrade was installed. The `CDF` Central Preshower and Crack Detector Upgrade consists of scintillator tiles with embedded wavelength-shifting fibers, clear-fiber optical cables, and multi-anode photomultiplier readout.

[8] The radiation length X_0 describes the characteristic amount of matter transversed by high energy electrons to lose by bremsstrahlung all but $1/e$ of their energy, which is equivalent to $7/9$ of the length of the mean free path for e^+e^- pair production of high energy photons. TThe average energy loss per unit of traversed material due to bremsstrahlung

Wall Hadronic calorimeters (`CHA` and `WHA` respectively), whose geometry tower segmentation matches the one used for the `CEM`, use 32 steel layers sampled each 2.5 cm (5 cm in the wall) by 1 cm thick acrylic scintillator. The total thickness of the hadronic section is approximately constant and corresponds to 4.5 interaction lengths (λ_0) [9]. A perspective view of a central electromagnetic calorimeter module (*wedge*) is shown in Fig. 2.7, where both the arrangement in projective towers and the light pipes of the electromagnetic compartment are shown.

The projective geometry has been used in order to better measure the overall transverse momentum of prongs in an event. Before the $p\bar{p}$ collision, the projection in the transverse plane w.r.t. the beam direction of the beam energy is zero, therefore this quantity must be the same after the collision. A significant unbalance in total transverse momentum is a measure of the transverse momentum carried away by neutrinos. For each tower the transverse energy E_T is defined as $E_T = E \sin\theta$, where E is the energy detected by the tower and θ is the angle between the beam axis and the projective tower direction. Two position detectors complement each wedge of `CEM`:

- The Central Electromagnetic Shower chamber (`CES`) is a two-dimensional strip-wire chamber located at maximum e.m. shower depth ($\sim 5.9X_0$). It measures the charge deposit of the electromagnetic showers, providing information on their pulse-height and position with a finer azimuthal segmentation than calorimeter towers. This results in an increased purity on electromagnetic object reconstruction. The `CES` purpose is to measure the position and the shape of electromagnetic showers in both transverse plane and longitudinal direction, which is used to distinguish electrons and photons from hadrons.

---

for an electron of energy E is related to the radiation length by $\left(\frac{dE}{dx}\right)_{brem} = -\frac{E}{X_0}$

[9] An interaction length is the average distance that a particle will travel before interacting with a nucleus: $\lambda = \frac{A}{\rho\sigma N_A}$, where A is the atomic weight, ρ is the material density, σ the cross section and N_A the Avogadro constant.

- The Central Pre-Radiator (CPR) consists of two wire chamber modules placed immediately in front of the calorimeter. It acts as a pre-shower detector by using the tracker and the solenoid coil material as radiators, resulting a very useful tools for distinguishing hadrons from electrons and photons.

Tab. 2.2 summarizes the basic parameters of the calorimeter detectors. The energy resolution for each calorimeter section was measured in the test beam and, for a perpendicularly incident beam, can be parametrized as

$$\frac{\sigma}{E} = \frac{\sigma_1}{\sqrt{E}} \oplus \sigma_2 \qquad (2.8)$$

where the first term comes from the sampling fluctuations and the photo-statistics of the PMTs (stochastic term), and the second term comes from the non-uniform response of the calorimeter (constant term). The symbol $\oplus$ indicates addition in quadrature.

2.4.2 The Plug Calorimeter

The plug calorimeter covers the $|\eta|$ region from 1.1 to 3.64. Both electromagnetic and hadronic sectors are divided in 12 concentric η-regions, with $\Delta\eta$ (η-width) ranging from 0.10 to 0.64, according to increasing pseudorapidity. Each of them is segmented in 48 or 24 (for $|\eta| < 2.11$ or $|\eta| > 2.11$ respectively) projective towers. The actual size of these towers was chosen so to have optimal separation of electron showers from the narrow forward hadron jets. Projective towers consist of alternating layers of absorbing material (lead and iron for electromagnetic and hadronic sectors, respectively) and scintillator tiles. The first layer of the electromagnetic tiles is thicker (10 mm instead of 6 mm) and made of material with higher photon yield. It acts as a pre-shower detector.

Calorimeter	CEM	CHA	WHA	PEM	PHA
Absorber	Lead	Steel	Steel	Lead	Iron
Segmentation ($\eta \times \phi$)	$0.1{\times}15$	$0.1{\times}15$	$0.1{\times}15$	$(0.1 \div 0.6){\times}(7.5 \div 15)$	$(0.1 \div 0.6){\times}(7.5 \div 15)$
Num. Towers ($\eta \times \phi$)	$20{\times}24$	$9{\times}24$	$6{\times}24$	$12{\times}24(48)$	$11{\times}24(48)$
Thickness	19 X_0, 1 ˘$_0$	4.7 ˘$_0$	4.7 ˘$_0$	23 X_0, 1 ˘$_0$	6.8 ˘$_0$
Resolution (%)	$14/\sqrt{E_T} \oplus 2$	$50/\sqrt{E_T} \oplus 3$	$75/\sqrt{E_T} \oplus 4$	$16/\sqrt{E} \oplus 1$	$80/\sqrt{E} \oplus 5$

Table 2.2 – Summary of the main parameters of the CDF II calorimeter system.

2.5 The Muon Chambers

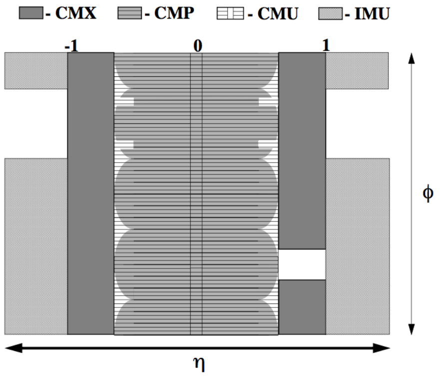

Figure 2.8 – Muon detectors coverage in the η-ϕ plane.

Parameter	CMU	CMP	CMX	IMU
Pseudorapidity range	$\lvert\eta\rvert < 0.6$	$\lvert\eta\rvert < 0.6$	$0.6 < \lvert\eta\rvert < 1.0$	$1.0 < \lvert\eta\rvert < 1.5$
Azimuthal coverage [°]	360	360	360	270
Maximum drift time [ns]	800	1400	1400	800
Drift tube cross section[cm]	2.68×6.35	2.5×15	2.5×15	2.5×8.4
Pion interaction length	5.5	7.8	6.2	62 - 20.0
Minimum $p_T(\mu)$ [GeV/c]	1.4	2.2	1.4	1.4-2.0

Table 2.3 – Design parameters of the muon detectors. See [24], [25].

Most particles produced in the primary interaction or in subsequent decays have a very high probability of being absorbed in the calorimeter system. Muons represent an exception. Muons do not interact via strong interaction with matter nuclei either. Therefore, a muon with enough energy will pass through the calorimeter systems releasing only a small amount of its energy[10]. At 90° the minimum muon energy needed to traverse the central

---

[10] Muons are over 200 times more massive than electrons, so *bremsstrahlung* radiation, inversely proportional to the mass squared of the incident particle, is suppressed by a factor

calorimeter and reach the first muon chamber is 1.4 GeV.

The muon system is the outermost layer of the CDF II detector and consists of four layers of drift cells and one layer of scintillation counters which are used to reconstruct track segments (*stubs*) of minimum ionizing particles and to provide accurate timing. Stubs are matched with the COT information in order to reconstruct the full trajectory of the muons. Four independent systems detect muons in the $|\eta| \lesssim 1.5$ pseudo-rapidity range reconstructing a small segment of their path (stub) sampled by the chambers, employing similar combinations of drift tubes, scintillation counters, and absorbers [24], [25]. The track momentum is found by pointing back the stub to the corresponding track bent in the COT. Scintillators serve as trigger and vetoes while the drift chambers measure the ϕ coordinate by drift time, and the z coordinate by charge division. All types of muon detectors use single wire, rectangular drift chambers, arranged in arrays with fine azimuthal segmentation and coupled with scintillator counters. The chambers use a 50:50 admixture of argon and ethane, and operates in proportional regime. The four sub-detector systems are (see Fig. 2.8):

CMU: the CMU detector is located around the central hadronic calorimeter at a radius of 347 cm from the beam-line with coverage $0.03 \lesssim |\eta| \lesssim 0.63$. It is segmented into 24 wedges of 15°. However, because of edge effects, only 12.6° of each wedge is active, resulting in an overall azimuthal acceptance of 84%. Each wedge is further segmented into three 4.2° modules each containing four layers of drift cells.

CMP: the CMP is a second set of muon drift chambers outside of CMU behind an additional 60 cm-thick steel absorber. The material further reduces the probability of hadronic punch-through to the CMP. Muons need a transverse momentum of about 2.2 GeV to reach the CMP. The CMP system is arranged in a box shape of similar acceptance as the CMU

---

of 4×10^4 with respect to electrons.

and serves as a confirmation of CMU for higher momentum muons. A layer of scintillation counters (CSP) is mounted on the outer surfaces of the CMP. The CMP and CMU have a large overlap in coverage and are often used together in indicating a muon track. CMP helps to cover CMU ϕ gaps and the CMU covers the CMP η gaps. Muon candidates which have both CMU and CMP stubs are the least contaminated by fake muons.

CMX: the CMX consists of drift tubes and scintillation counters (CSX) arranged in truncated conical shape. The CMX extends the pseudo-rapidity coverage to $0.6 \lesssim |\eta| \lesssim 1$. There are 8 layers of drift chambers in total, with a small stereo angle between layers.

IMU: the IMU extends the pseudo-rapidity coverage even further to $1.0 \lesssim |\eta| \lesssim 1.5$. The IMU is mounted on the toroid magnets, which provide shielding.

Tab. 2.3 summarizes a few relevant design parameters of the detectors.

2.6 CLC detector

Absolute measurements of the instantaneous luminosity by the machine, based on beam parameters measurements, have uncertainties of the order of 15-20%. For this reason in CDF the collider luminosity is determined from the observed interaction rate in a detector whose covered cross section can be reliably computed. The measurement is made by gas Cherenkov counters (CLC) located in the pseudorapidity region $3.7 < |\eta| < 4.7$, which measure the average number of inelastic interactions per bunch crossing.
Each module consists of 48 thin, gas-filled, Cherenkov counters. The counters are arranged around the beam pipe in three conical layers, with 16 counters each pointing to the center of the interaction region. The cones in

the two outer layers are about 180 cm long and the inner layer counters, closer to the beam pipe, have a length of 110 cm. This geometry allows detecting only particles produced at the collision point. The total signal of the counters allows separating forward inelastic interactions from background and deriving the collider luminosity from their observed rate.

2.7 The CDF Trigger System

$p\bar{p}$ collisions at Tevatron happen with a frequency of 2.5 MHz (i.e every 396 ns). The bunch-bunch luminosity and the interaction cross-section are such that in average one or a few interactions take place at each bunch crossing. With an average event size of $\sim$ 250 kb, this represents a huge amount of data which would flow through the CDF data acquisition system (DAQ). The CDF DAQ can sustain only a small fraction of this data flow, since the maximum rate for storing data to disk is $\sim$ 75 Hz.

The trigger is the system devoted to perform a quick online selection and keep only the events interesting for physics. A rejection factor of 10000 is needed to match the DAQ capabilities. As shown in Fig. 2.9, the CDF trigger is implemented in three levels of successively tighter and more sophisticated event selection. The first level is hardware based; the second is a mixture of hardware and software, and the third is purely software, implemented in an on-line computer cluster.

2.7.1 LEVEL 1

At LEVEL 1 the decision logic is implemented in hardware: the selection algorithms are hard-coded into the electronic circuits of the trigger boards. In a synchronous pipeline up to 42 subsequent events can be stored for $\sim$ 5.5 μs while the hardware is making a decision. If no acceptance decision is made within that time the event is lost. L1 decision are made on average in

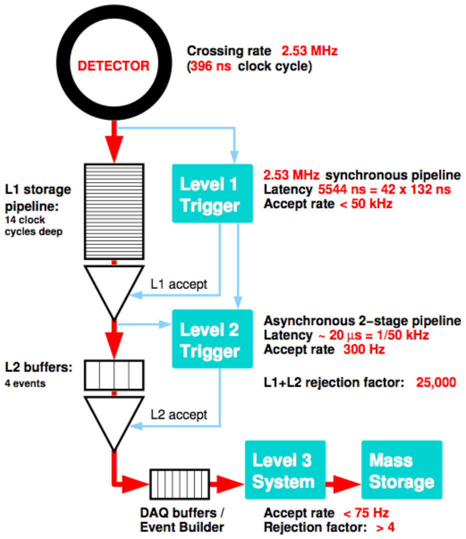

Figure 2.9 – Functional block diagram of the CDF II trigger and data acquisition systems.

about 4 μs: no dead time is expected from this level. Level 1 rejects 97% of the events, by reducing the event rates from 2.53 MHz to less than 40 kHz. The L1 decision is generated using information from:

- XFT (extremely fast tracker), which reconstructs approximate tracks ($p_T > 1.5$ GeV/c) in the transverse plane by exploiting information from COT superlayers. These tracks are extrapolated to the calorimeters and muon chambers to contribute to all trigger levels;
- the calorimeter towers, which carry information on the electromagnetic and hadronic energy deposits (*seeds*, which can initiate electron/photon or jet identification);
- the *muon stubs* (segment of tracks reconstructed in the muon chambers), which are matched to the XFT tracks.

The XFT is a custom processor used to reconstruct two-dimensional tracks in the (r, ϕ) plane in the COT. The XFT is capable of reconstructing tracks with $p_T \gtrsim 1.5$ GeV/c with an efficiency of about 95% and a fake rate of a few percent. The XFT has an angular segmentation of 1.25°, and an angular resolution of 0.3°. The momentum resolution is $\sigma_{p_T}/p_T^2 \approx 0.017\ (\mathrm{GeV}/c)^{-1}$. XFT sends the tracks to an extrapolation unit (XTRP) feeding three L1 elements: L1CAL, L1TRACK, and L1MUON. L1CAL and L1MUON use extrapolated tracks and information from the calorimetry and muon systems respectively to search for possible electron, photon, jets and muon candidates. A decision stage combines the information from these low-resolution physic objects, called *primitives*, into more sophisticated objects.

2.7.2 LEVEL 2

LEVEL 2 is an asynchronous system which processes events that have received a L1 accept in a FIFO (First In, First Out) manner. It is structured as a two stage pipeline with data buffering at the input of each stage. The first stage is based on dedicated hardware processors which assemble information from a particular section of the detector. The second stage consists of a computer which uses the list of objects generated by the first stage and implements in software the event selection. Each of the L2 stages is expected to take approximately 10 μs with a latency of approximately 20 μs. The input buffers can store up to four events. After the LEVEL 2, the event rate is reduced to about 1 KHz (rejection factor ~ 40). The purposes of L2 are:

- to cluster the energy deposited in the towers around L1 seeds, as an approximate measure of electron, photon or jet energy;
- to use calorimeter and CES chamber information to improve separation of $e^{\pm}$ and γ from hadrons;
- to improve the matching between XFT tracks and muon stubs in order to have a better muon signature;
- to provide a measurement of the track impact parameters by means of the Silicon Vertex Trigger element (SVT), which allow to select events

with secondary vertices from decay of long-lived heavy-flavour hadrons.

The SVT uses SVX r-ϕ hits to extend XFT track primitives inside the SVX volume, closer to beam-line. The SVT improves the XFT ϕ_0 and p_T resolutions and allows to measure the impact parameter d_0 (original XFT track primitives are beam-line constrained).

2.7.3 LEVEL 3

LEVEL 3 is a software trigger. It is operated on a cluster of ~ 300 processors which reconstruct the entire event with the same accuracy as in the off-line analysis. The final decision to accept an event is made on the basis of a list of observables indicating candidate events of physical interest (top quark production events, W/Z events, Drell-Yan events, ...). Events that satisfy the Level 3 trigger requirements are transferred onward to the Consumer Server/Data Logger (CLS) system for storage first on disk and later on tape. The average processing time per event in Level 3 is in the order of 1 s. The Level 3 leads to a further reduction in the output rate, with an accepted maximum of about 200 Hz.

2.7.4 Trigger Paths

A set of requirements that an event has to fulfill at Level 1, Level 2 and Level 3 constitutes a *trigger path*. The CDF II trigger system implements about 150 trigger paths, which are periodically adjusted depending on machine luminosity and physics needs.

An event will be accepted if it passes the requirements of any one of these paths. The trigger system described above exploits the information of all detector subsystems. Combining the measurements of the various subsystems it is possible to efficiently record, events characterized by different signatures.

Triggers which use a bandwidth fraction larger than the assigned one are *prescaled*. A trigger path is said to be prescaled by a factor N if it is configured to accept only one event out of N input events. Prescaling is dynamically implemented by luminosity-dependent factors during data taking. This is important in order to ensure that no trigger path reaches rates so high as to create unacceptable dead time to triggers on rare events of primary importance. During data taking the luminosity decreases with time, and consequently a number of prescale factors can be relaxed. The prescale factors decrease proportionally to the rate of triggered events, so as the number of recorded events is constant. Using dynamic prescaling ensures that optimal use for physics is made of the available luminosity.

The accepted events are recorded on tape and organized in *data sets* according to the trigger path they satisfy.

Chapter 3

Reconstruction of Physical Objects

Particles generated in $p\bar{p}$ collisions are identified using the information provided by the `CDF` sub-detectors described in the previous chapter. The unprocessed output from the `CDF` detector is a series of electronic signals recorded by the hardware components, which must be converted into physical information. From the raw data, high-level objects (such as tracks, vertices, calorimeter clusters) are reconstructed and combined to identify physical objects (electrons, muons, neutrinos and jets) of interest for the analysis. The ability to detect and reconstruct the trajectories of charged particles is essential for particle identification and momentum measurement.

3.1 Track Reconstruction

Charged particles traveling through a homogeneous solenoidal magnetic follow helical paths around the z-direction.

Knowing that the projection of the helix on the x-y plane is a circle, five parameters are needed to uniquely parameterize a helix in three dimensions:

C – signed helix (half)-curvature, defined as $C = q/2R$, where R is the radius of the helix and q is the particle charge. This is directly related to the transverse momentum. If the magnetic field B is measured in T, C in m^{-1} and p_T in GeV/c, then $p_T = 0.15\, qB/|C|$.

ϕ_0 – ϕ azimuthal angle of the particle trajectory at the point of closest approach to the z-axis.

d_0 – signed impact parameter, i.e. the radial distance of closest approach to the z-axis. defined as $d_0 = q(\sqrt{x_0^2 + y_0^2} - R)$, where (x_0, y_0) are the coordinates of the center. This is schematically drawn in section 2.3.

λ – helix pitch, i.e. $\cot(\theta)$, where θ is the polar angle of the particle at the point of its closest approach to the z-axis. This is directly related to the longitudinal component of the momentum: $p_z = p_T \cot\theta$.

z_0 – the z coordinate of the point of closest approach.

Another useful quantity is L_{xy}, the displacement of the secondary vertices of decaying particles in the transverse plane, defined as

$$L_{xy} = \frac{\widehat{x}_V \cdot \vec{p}_T}{|p_T|}, \tag{3.1}$$

where $\widehat{x}_V$ is the decay vertex position in the transverse plane.
The trajectory of a charged particle satisfies the following equations

$$\begin{aligned} x &= \quad r\sin\phi - (r - d_0)\sin\phi_0 \\ y &= -r\cos\phi + (r + d_0)\cos\phi_0 \\ z &= z_0 + s\lambda \end{aligned} \tag{3.2}$$

where s is the projected length along the track, $r = 1/2C$ and $\phi = 2Cs + \phi_0$. The reconstruction of a charged particle trajectory consists in determining the above parameters through an helical fit of a set of spatial measurements (*hits*) reconstructed in the tracking detectors by clustering and pattern-recognition algorithms. The helical fit takes into account field non-uniformities and scattering by the detector material. All tracks are first fit in the COT and then extrapolated inward the silicon. This approach guarantees fast and efficient tracking with high tracks purities. The greater radial distance of the COT with respect to the silicon tracker results in a lower track density and consequent fewer accidental combination of hits in the track reconstruction. For more details see [33], [34].

3.1.1 Primary Vertex Reconstruction

The primary vertex position for a given event is found by fitting high quality tracks to a common point of origin. At high luminosities, multiple collisions occur in a given bunch crossing. For a luminosity of 10^{32} cm^{-2}s^{-1}, there is an average of 2.3 interactions per bunch crossing. Typically, since the luminous region is sufficiently long (with $\sigma_z = 29$ cm), the primary vertices associated to the collisions are well separated in z. An iterative algorithm is used to find the vertex associated to the hardest collision: the first estimate of its position (x_V, y_V, z_V) is binned in the z coordinate, then the z position of each vertex is calculated from the weighted average of the z coordinates of all tracks within 1 cm of the first iteration vertex, with a typical resolution of 100 μm; finally the vertex associated with the highest sum of the tracks p_T is defined as primary vertex of the event.

The locus of all primary vertices defines the beam-line, the position of the luminous region of the beam-beam collisions through the detector. The beam-line is used as a constraint to refine the knowledge of the primary vertex in a given event. Typically the beam transverse section is circular with a width of $\sim$ 30 μm at $z = 0$, rising to $\sim$ 50-60 μm at $|z| = 40$ cm. The beam at the interaction point is not necessarily parallel to the detector axis nor centered in the detector, and moves the beam line by fractions of millimeter as a function of time.

3.2 Lepton Reconstruction and Identification

Lepton reconstruction depends on the type of lepton and its direction inside the detector. Although this work focuses on a final state containing large $\not{E}_T$ and hadronic jets, lepton identification is still essential, since in order to ensure statistical independence with analyses containing a lepton in the final state, one of the requirements applied to the preselection sample is to reject events with a reconstructed lepton (*lepton veto).*

In the following, we briefly describe how leptons are identified at CDF; in particular, the categories we use in this analysis are the Central Electrons, the Plug electrons and the Central Muons. The quantities used to identify lepton candidates are:

- the total transverse energy of the electron cluster in the electromagnetic calorimeter E_T;
- p_T, the track transverse momentum;
- the ratio of the total hadronic cluster energy to the EM energy $E_{\mathrm{had}}/E_{\mathrm{em}}$;
- the position of the track vertex along the z-axis, Z;
- the number of axial superlayers containing a signal, AS, and the number of hits per superlayer, hpAS;
- the number of stereo superlayers containing a signal, SS, and the number of hits per superlayer, hpSS;
- the distance between the PES centroid and the PEM centroid, ΔR_{plug};
- the track impact parameter respect to the primary vertex d_0;

- the ratio of the energy collected in 5 layers over the energy collected in 9 layers of the PES, in the u and v orthogonal directions, PES_5x9_u and PES_5x9_v;
- the track isolation Iso4, defined as the scalar sum of transverse energies of the tracks in a cone radius $\Delta R = \sqrt{(\Delta\eta)^2 + (\Delta\phi)^2} < 0.4$ around the lepton candidate track;
- The χ^2 resulting from the comparison of the PEM shower profile of the electron candidate with the profile of test beam electrons, using a (3×3) cluster size, χ^2 (3×3)
- the matching between the candidate muon track and a stub in the CMU/CMP/CMX.

Central Electrons	
E_T	≥ 20 GeV
p_T	≥ 10 GeV
$E_{\text{had}}/E_{\text{em}}$	$< 0.055 + (0.00045 \times E)$
$\lvert Z \rvert$	≤ 60 cm
AS, hpAS	$> 3, 5$
SS, hpSS	$> 2, 5$
Iso4/p_T	< 0.1
Plug Electrons	
E_T	≥ 20 GeV
$E_{\text{had}}/E_{\text{em}}$	$< 0.055 + (0.00045 \times E)$
PES_5x9_u	≥ 0.65
PES_5x9_v	≥ 0.65
Iso4/p_T	< 0.1
χ^2 (3×3)	< 10
ΔR_{plug}	< 3 cm

Table 3.1 – Central and Plug electrons identification criteria.

3.2.1 Electrons

Electrons are identified by the electromagnetic calorimeters CEM and PEM. The identification selections are different for CEM and PEM, and are listed in table 3.1. Electron candidates identified in the central calorimeter must also match a track in the `COT`. The efficiencies of electron identification cuts are 0.923 ± 0.001 and 0.837 ± 0.003 respectively for central and plug electrons. Fake rates are in the order of a few %.

3.2.2 Muons

We form muon candidates by matching a track to stubs in the muon chambers. All events are required not to pass a cosmic tag. Furthermore, to reject hadrons the energy deposited in the calorimeter by the candidate track is required to be consistent with that of minimum ionizing particles. Finally, an isolation requirement is applied, in which the energy in the cone is compared to the track p_T. All requirements are listed in table 3.2. The efficiencies of these cuts are 90.52 ± 0.37 and 92.75 ± 0.47 respectively for CMUP and CMX. Also for muons, fake rates are in the order of a few %.

Central Muons	
p_T	≥ 20 GeV
E_{em}	< 2 GeV + $\max(0, 0.0115 \times p - 100)$
E_{had}	< 6 GeV + $\max(0, 0.028 \times p - 100)$
$E_{\text{had}}/E_{\text{em}}$	$< 0.055 + (0.00045 \times E)$
$\lvert Z \rvert$	≤ 60 cm
AS, hpAS	$> 3, 5$
SS, hpSS	$> 2, 5$
$\lvert d_0 \rvert$ (with silicon hits)	< 0.02 cm
$\lvert d_0 \rvert$ (with no silicon hits)	< 0.2 cm
$\mathsf{Iso4}/p_T$	< 0.1
ΔX(CMU) (if CMUP)	< 7 cm
ΔX(CMP) (if CMUP)	< 5 cm
ΔX(CMX) (if CMX)	< 6 cm

Table 3.2 – Central muons identification criteria.

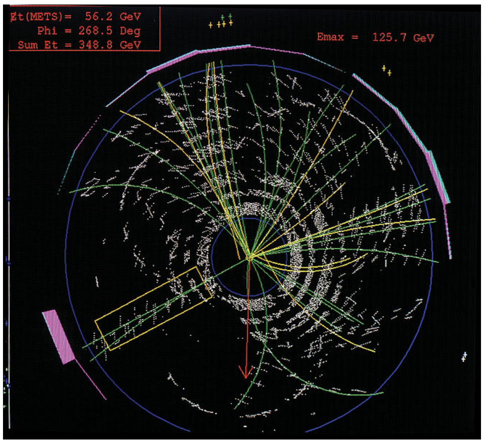

Figure 3.1 – Candidate $t\bar{t}$ pair decaying into jets, visible as collimated collections of particle tracks, and other fermions in the CDF detector.

3.3 Jet Reconstruction

The scattered-out quarks and gluons undergo the hadronization process, which produces collimated bunches of colorless hadrons (*jets*) which keep track of the energy and the direction of the originating parton. From the experimental point of view, the resulting shower of particles appears as a large energy deposit in a localized area of the detector (Fig. fig. 3.1). The challenge is to recover from the detector information the initial energy, the momentum and, possibly, the nature of the parton originating the jet. To reconstruct jets, CDF developed several different reconstruction algorithms [37].

3.3.1 JETCLU algorithm

The most common et reconstruction algorithm used at CDF is a *cone algorithm* named JETCLU [38], which consists of three steps. In the first step preclusters are built from adjacent *seed towers* (calorimeter towers with $E_T >$ 1 GeV). The size of these preclusters is limited to $2R_{\text{cone}} \times 2R_{\text{cone}}$ in the η-ϕ plane, where R_{cone} is the parameter of the jet algorithm which controls the size of the jets.

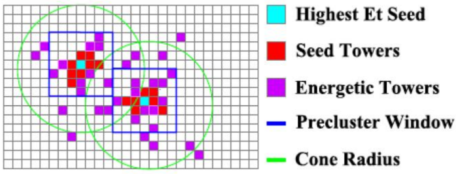

Figure 3.2 – Illustration of jet clustering by the JETCLU algorithm.

After that, for each precluster a cone is defined by all seed towers inside the precluster and all towers with $\Delta R = \sqrt{\Delta\eta^2 + \Delta\phi^2} < R_{\text{cone}}$ with respect to the highest jet energy tower. The centroids of the cones are calculated. The identification of the members of the cones and the calculation of their centroids is repeated until the old centroids (the cone axes) agree with the new ones.

In a last step overlapping stable cones have to be reconsidered because each calorimeter tower may only belong to one jet. A pair of overlapping cones is merged if more than 75% of the transverse energy of one of the cones is shared by the other one. Otherwise they are separated using an iterative algorithm. The towers are redistributed to the cone whose centroid is closest and the centroids are recalculated until a stable configuration is reached.

The transverse energy and the position of the reconstructed jet are then given by:

$$E_T^{\text{jet}} = \sum_i E_T^i \tag{3.3}$$

$$\eta = \frac{1}{E_T^{\text{jet}}} \sum_i E_T^i \eta^i \tag{3.4}$$

$$\phi = \frac{1}{E_T^{\text{jet}}} \sum_i E_T^i \phi^i \tag{3.5}$$

where E_T^i, η_i and ϕ_i are the trasnverse energy and the position of the i-th tower.

3.3.2 Jet Energy Corrections

The four-momentum assigned to a jet must be corrected to account for detector defects and reconstruction algorithm imperfections. In order to convert the measured transverse jet energy into the transverse energy of the partons, a set of corrections to the measured jet energy (*raw energy*) have been developed.

The corrections, developed using data and simulation of the `CDF` detector, address the response inhomogeneity in η, the contributions from multiple interactions, the non-linearity of the calorimeter response, the contribution by the underlying event (particles emitted in the event but not belonging to the hard interaction) and the jet energy flow out of the jet cone.

Each of those corrections has a fractional uncertainty, $\sigma_{JES}(p_T)$ which can be parameterized as a function of the corrected transverse momentum of the jet p_T.

They are applied in a sequence of *L-levels* in order to correct for each bias independently [39].

The correction can be parameterized as follows

$$p_T^{\text{parton}} = (p_T^{jet} \cdot C_\eta - C_{MI}) \cdot C_{Abs} - C_{UE} + C_{OOC} = p_T^{\text{particle}} - C_{UE} + C_{OOC},$$

where the terms are described below.

C_η: pseudorapidity-dependent correction (L1)

The L1 corrects for non-uniformities in calorimeter response along η. It is obtained by studying the p_T balancing in dijet events, which are selected in order to have one jet ("trigger jet") in the $0.2 < |\eta| < 0.6$ region (far away from detector cracks). The other jet, called "probe jet", is free to span over the entire $|\eta| < 3$ region.

Since in a perfect detector the two jets must be balanced in p_T, a balancing

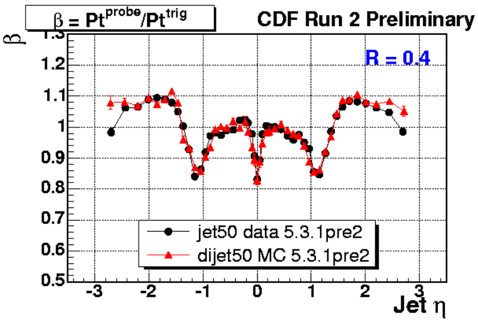

Figure 3.3 – η-dependent energy-scale correction factor for JETCLU with radius 0.4; a sample of events with at least one trigger tower above 50 GeV is used.

fraction is formed

$$f_b = \frac{\Delta p_T}{p_T^{ave}} = 2 \cdot \frac{p_T^{probe} - p_T^{trigger}}{p_T^{probe} + p_T^{trigger}}$$

The average of f_b in the analyzed η bin is used to define the β_{f_b} factor[1] (see fig. 3.3)

$$\beta_{f_b} = \frac{2 + \langle f_b \rangle}{2 - \langle f_b \rangle} \tag{3.6}$$

The final L1 correction is defined as $f_{L1}(\eta, E_T^{raw}, R) = 1/\beta_{f_b}$ and the uncertainty associated with this correction is estimated to be of the order of 1% for central jets and 7.5% for forward jets.

C_{MI}: multiple interactions correction (L4)

The number of interactions occurring during beam bunch crossings follows a Poisson distribution whose mean increases with instantaneous luminosity.

These additional interactions, dominantly soft *minimum bias* events, cause extra unwanted energy to be deposited within the jet cone.

---

[1] The definition of eq. (3.6) is in average equal to $p_T^{\text{probe}}/p_T^{\text{trigger}}$ but it reduces the sensitivity to the presence of non-Gaussian tails which affect the $p_T^{\text{probe}}/p_T^{\text{trigger}}$ ratio.

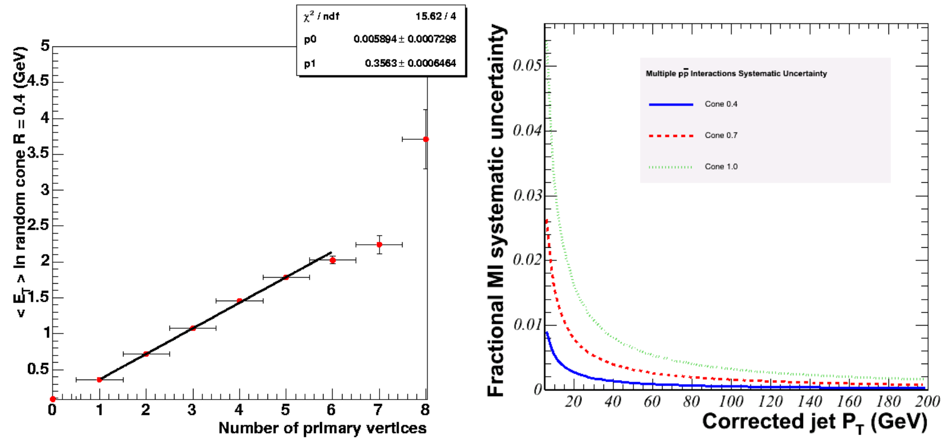

Figure 3.4 – (a) E_T in R=0.4 cone as a function of the number of reconstructed primary vertexes in minimum bias events. (b) fractional systematic uncertainties due to multiple interactions for different cone sizes as a function of jet transverse momentum.

L4[2] correction takes into account the number of reconstructed vertices to estimate the effect. The average energy flow in minimum bias events, which are triggered by the luminosity monitor CLC, is measured in the best-performing region ($0.2 < |\eta| < 0.6$) of the calorimeter as a function of the number of reconstructed vertices. The resulting plot is fit to a straight line (see fig. 3.4). This is used to correct in average the energy of the jets. Because of the finite reconstruction efficiency of the vertices, this linear approximation works well for events with less than seven vertices.

This is not a serious limitation because in practice events with so many vertices are very rare. The uncertainty on this correction is estimated to be of the order of 15%.

C_{Abs}: absolute energy scale corrections (L5)

While L1 and L4 are corrections at calorimeter level, L5 steps back to particle level. The procedure used to estimate the L5 correction factor is described accurately in [39]. It uses a MC sample of inclusive dijet events

---

[2] L2 and L3 have survived in the CDF jargon but are not used anymore.

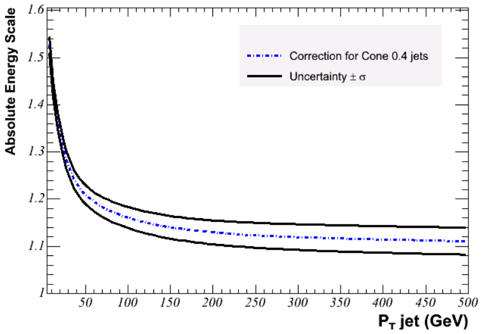

Figure 3.5 – Absolute energy corrections for jets with cone size $\Delta R = 0.4$ as a function of jet p_T (dotted), with 1σ uncertainty bands (full).

simulated with PYTHIA [41].

The correction is derived comparing particle jets at generator level (before they are passed through the detector simulation), with calorimeter jets, as obtained from the detector simulation. Generated and calorimeter jets are required to be within 0.1 of each other in the $\eta - \phi$ plane to ensure that they are the same object. The probability at the distribution maximum of measuring a value of p_T^{jet} given p_T^{particle} is taken as a correction factor (see fig. 3.5). The uncertainty on this corrections is estimated to be of the order of 3.5% (15% near the edge of the calorimeter).

C_{UE} and C_{OOC}: underlying event (L6) and out-of-cone (L7) corrections

Reconstructed jet energies in hard $p\bar{p}$ interactions may contain contributions by particles created by interactions involving other partons in the colliding hadrons (spectator interactions) or by gluons from initial state radiation in the hard interaction. These contributions are called *underlying event*. On the other hand, a fraction of the parton energy may be lost outside the jet cone because of final state gluon radiation, fragmentation at large angles relative to the jet axis or low p_T particles bending out of the jet cone in the magnetic field. This energy is modeled imperfectly in MC events, so the correction factor and its systematic uncertainty are assigned by examining photon + jets events in data and MC. A ring around the jet with a radius between 0.4 and 1.3 in the $\eta - \phi$ plane is examined, and the energy in this region is compared between data and MC simulation. The largest difference between MC events and data is taken as a systematic uncertainty.

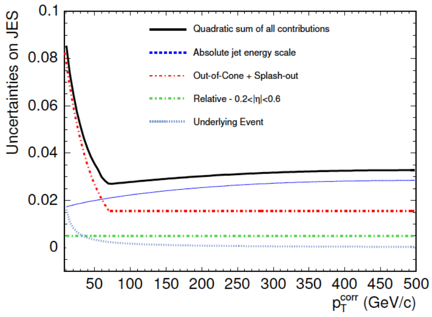

Figure 3.6 – The fractional systematic uncertainty of the JES corrections as a function of the jet transverse momentum. The total uncertainty is taken as the sum in quadrature of all individual contributions.

fig. 3.6 shows the individual fractional systematic uncertainties as a function of jet p_T in the central region, $0.2 < |\eta| < 0.6$, of the calorimeter. They are independent of each other and thus are added in quadrature to derive the total uncertainty.

C_{qg}: quarks and gluons corrections (L9)

L9 jet energies corrections are based on the initial parton type originating the jet. The procedure used to estimate the L9 corrections is fully described in [40]. Differences between quark and gluon jet energy scales are not well modeled in ALPGEN + PYTHIA Monte Carlo simulations. It is possible to derive separate corrections for quark jets and gluon jets in data and MC given two independent samples of jets, with different known quark fractions, balanced against objects of known energy. To derive a correction for Monte Carlo, Z-jet (rich in gluons) and γ-jet (rich in quarks) samples are used. Rather than deriving full and separate jet energy corrections for data and MC, the balance in data and MC in Z-jet and γ-jet is compared:

$$K_{Z/\gamma} = (E_T^{jet}/p_T^{Z/\gamma}) - 1 \tag{3.7}$$

From this comparison, an additional correction to be applied to MC jets (on top of the L5 or L7 corrections) based upon whether they are quarks or gluons, in order to better match the data, is found. Quark jet energies, at L5 or L7, should be corrected upwards by $\sim$ 1%, while gluon jet energies should be corrected downwards by $\sim$ 7%. These corrections are are found to be approximately independent of the jet energy for energies $\gtrsim$ 15 GeV.

3.4 Missing Transverse Energy

Protons and antiprotons that collide at the Tevatron have equal and opposite momenta. Therefore, the total vector momentum sum in an event should be zero. The hard collision happens between the partons of the proton and antiproton, and they can carry any fraction of the parent proton or antiproton. Since the hard collision takes place between single partons whose fractional momenta are unknown, conservation of longitudinal momentum cannot be exploited. However, primary partons carry a very limited transverse momentum[3], and the total transverse momentum in the final state can be assumed to be approximately zero. Any transverse energy imbalance in the detector may indicate that a particle left the detector without interacting with its material.

In this analysis, we select events with large missing transverse energy in the final state; therefore, a deep understanding and an accurate reconstruction of this quantity are extremely important.

The x and y components of the raw missing transverse energy of the event

---

[3] of the order of 0.1 GeV/c, as associated to their Fermi motion inside the protons.

are defined as

$$\not{E}_x = - \sum_{i}^{\text{towers}} E_T^i \cos\phi_i \tag{3.8}$$

$$\not{E}_y = - \sum_{i}^{\text{towers}} E_T^i \sin\phi_i, \tag{3.9}$$

where the sum is taken over all towers that are above a threshold of 0.1 GeV, and the total electromagnetic and hadronic energy in the i^{th} tower is E_T^i.

The magnitude of the missing energy and its azimuthal direction are then calculated as

$$\not{E}_T = \sqrt{\not{E}_x{}^2 + \not{E}_y{}^2} \tag{3.10}$$

$$\phi(\not{E}_T) = \arctan\left(\frac{\not{E}_y}{\not{E}_x}\right) \tag{3.11}$$

3.4.1 Fake Missing Transverse Energy

While a large $\not{E}_T$ is legitimately observed in events that contain particles that do not interact with the detector, there are several effects that may also lead to the experimental signature of $\not{E}_T$. ne must apply as accurate corrections as possible for each one of them:

- problems with some of the calorimeter tower electronics/calibrations may cause the tower to report a wrong value of the energy of the incident particles;

- when the direction of an energetic jet is near an uninstrumented calorimeter region, the energy of the jet will be underestimated. A configuration of two jets that are produced back-to-back with the same momentum will appear to have a momentum imbalance;

- when protons or antiprotons of the Tevatron beam collide with nuclei of gas atoms or beam collimators, they produce a *halo* of muons, travelling roughly parallel to the beam. Some of these muons cross a row of calorimeter towers along the z-axis depositing energy to the calorimeters asymmetrically in ϕ;

- muons carrying a large momentum can be created in the hard collision. Being minimum ionizing particles, these muons can pass through the calorimeter, without substantial energy loss;
- cosmic muons traveling through the detector;
- proton or antiproton beam remnants and beam losses in very forward regions.

3.4.2 $\not\!\!E_T$ corrections

The $\not\!\!E_T$ measured by the CDF calorimeter (*raw* $\not\!\!E_T$) needs to be corrected for the same reasons that the jet energies do, as described in section. Hence, the $\not\!\!E_T$ needs to be recomputed using the corrected values of the jet energies. The event $\not\!\!E_T$ is thus corrected using the corrected E_T^{corr} values, according to the formulas

$$\not\!\!E_x{}^{\mathrm{corr}} = \not\!\!E_x{}^{\mathrm{raw}} - \sum_i^{\mathrm{jets}} \left(E_x^{\mathrm{corr},i} - E_x^{\mathrm{raw},i} \right) \tag{3.12}$$

$$\not\!\!E_y{}^{\mathrm{corr}} = \not\!\!E_y{}^{\mathrm{raw}} - \sum_i^{\mathrm{jets}} \left(E_y^{\mathrm{corr},i} - E_y^{\mathrm{raw},i} \right) \tag{3.13}$$

The azimuthal direction of the corrected $\not\!\!E_T$ is also corrected:

$$\phi(\not\!\!E_T{}^{\mathrm{corr}}) = \arctan\left(\frac{\not\!\!E_y{}^{\mathrm{corr}}}{\not\!\!E_x{}^{\mathrm{corr}}} \right) \tag{3.14}$$

The $\not\!\!E_T$ energy used everywhere in this analysis is the corrected $\not\!\!E_T$.

3.5 Reconstruction of the Secondary Vertex: b-Jets Identification

A fundamental tool in collider physics is the identification of jets coming from heavy flavour quarks, i.e. bottom or charm hadrons. For example, determining (*tagging*) the b-flavour of jets is extremely important in the study of top quark physics.

Heavy flavor jets can be identified by an observable *secondary vertex* inside a jet cone. Immediately after their formation, regardless of the particular production process, b quarks undergo *hadronization*, forming a colorless B hadron (either a B mesons, such as B^0, $B^{\pm}$ or B_s^0, or a B baryon such as the Λ_b), which usually carries most of the momentum of the original b quark. Later on, B hadrons decay with a lifetime of $\sim$ 1.6 ps which, together with a large relativistic boost, results in a decay length of the order of several millimeters, which is distant enough from the primary vertex to be correctly identified by the detector[4].

The B hadrons decays produce sub-jets composed by tracks with large impact parameter d_0, i.e. with low probability of coming from the primary vertex. The impact parameter is reconstructed by the silicon detector with a precision of $\approx 50\ \mu$m, making it possible to separate displaced tracks from prompt tracks coming from the primary interaction, as shown in fig. 3.7 for a W + jets event with two displaced secondary vertices.

Both b-taggers used in this analysis, `SecVTX` and `JetProb`, are based on algorithms that perform secondary vertex reconstruction using information on the tracks inside the jet. An overview of each method is presented in the following.

---

[4] For example, the mean transverse momentum of a B hadron coming from a single-top s-channel process is $\sim$ 50 GeV/c. Since B-hadrons have a mass of $\sim$ 5 GeV/c^2, it undergoes a boost of $\beta\gamma \sim 10$. Accordingly, the impact parameter of each secondary vertex track can easily be of the order of 1 mm.

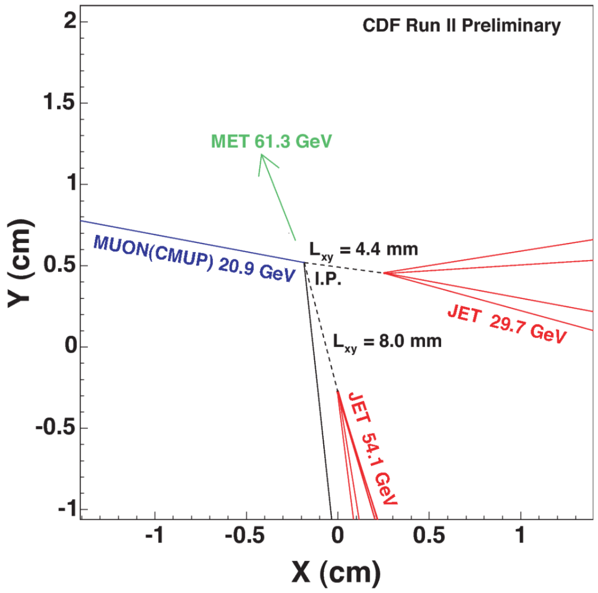

Figure 3.7 – W + jets candidate event with two secondary vertices tagged by SecVTX (run 166063, event 279746). The $\not{E}_T$ direction, a muon track, a prompt track and tracks from the secondary vertices are shown

3.5.1 The SecVTX algorithm

The SecVTX algorithm searches for secondary vertices using the tracks within the jet cone of radius $\Delta R = 0.4$ (i.e. with $\Delta R(\text{jet}, \text{trk}) < \Delta R$), selecting tracks with large d_0 with respect to the primary vertex, in a fiducial region of $|d_0| < 1.5$ mm, and trying to merge them into a common vertex.

Tracks passing certain requirements ($p_T > 0.5$ GeV$/c$, $d_0/\sigma_0 > 2.0$) are defined as *usable*, while a jet containing at least 2 usable tracks is defined as *taggable*. The algorithm uses a two-pass approach to find secondary vertices: the first pass attempts to reconstruct a secondary vertex including at least three tracks with $d_0/\sigma_0 > 2.5$ and at least one with $p_T > 1.0$ GeV$/c$; the second is performed in case of negative pass-1 result and requires only two tracks but with $d_0/\sigma_0 > 3.5$, one track with $p_T > 1.5$ GeV$/c$ and the other one with $p_T > 1.0$ GeV$/c$. If a secondary vertex is found in a jet, the jet is defined as SecVTX *tagged*.

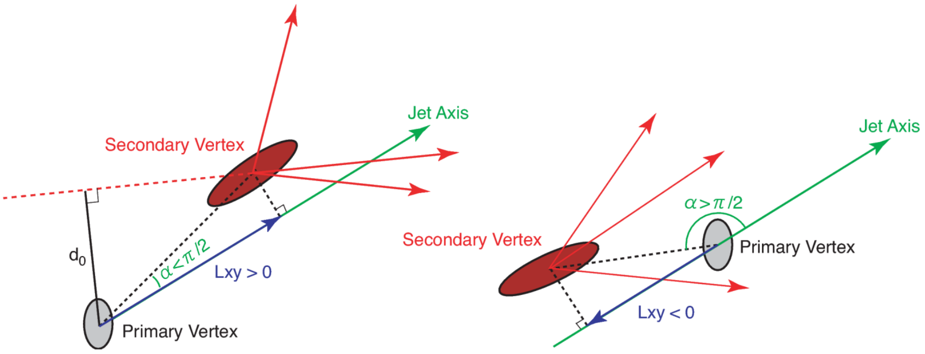

Figure 3.8 – Left: true reconstructed secondary vertex. Right: negative SecVTX tag, falsely reconstructed secondary vertex

The two-dimensional decay length of the secondary vertex L_{xy} is calculated as the projection into the jet axis, in the (r, ϕ) plane, of the vector pointing from the primary vertex to the secondary vertex. The sign of L_{xy} is defined by the angle α between the jet axis and the SecVTX vector, being positive if $\alpha < \pi/2$ and negative if $\alpha > \pi/2$, as shown in fig. 3.8.

Events containing heavy flavour hadrons, i.e. with tagged jets, are expected to have secondary vertices with large positive L_{xy}. To reduce background from mismeasured tracks, a cut on $|L_{xy}/\sigma_{xy}| > 7.5$ is required. Negative tags are due to the finite tracking resolution of the CDF tracking system, but are not rejected since they are useful to calculate the false positive (*mistag*) tag rate.

3.5.2 Tagging Performance and Scale Factors

The performance of a b-tagger is judged considering its *efficiency*, i.e the rate of correctly identified B hadrons over all the produced B hadrons, and on its *purity*, i.e the rate of falsely identified B hadrons in a sample with no true B hadrons (mistags). CDF uses Monte Carlo simulations to evaluate SecVTX efficiency. In fig. 3.9 the b-tagging efficiency is plotted as a function of jet η, E_T and the number of vertices for two SecVTX modes *tight* and *loose*.

The drop in tagging efficiency at large η is due essentially to lower track reconstruction efficiency.

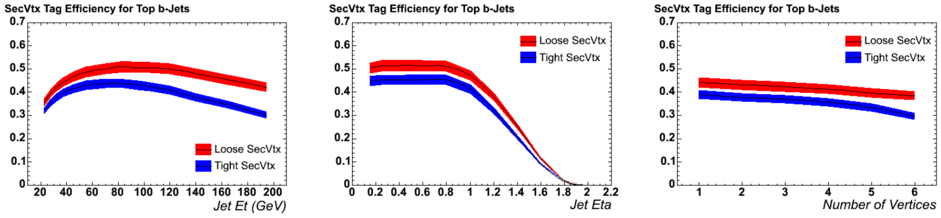

(a) (b) (c)

Figure 3.9 – b-tagging efficiency for the two operation modes of the SecVTX algorithm vs η (a), E_T (b), nVtx (c).

Since Monte Carlo simulations do not reproduce the exact b-tagging efficiency of SecVTX, a *scale factor* Φ [43] is introduced to account for the data/MC difference in the form of the ratio $\Phi \equiv \varepsilon_{\text{data}}/\varepsilon_{\text{MC}}$. The tagging efficiency is calculated by multiplying the tag rate of jets matched with heavy-flavour quarks by the data/MC scale factors that are listed for the three modes in table 3.3.

mode	Φ	$\sigma_\Phi(stat)$	$\sigma_\Phi(syst)$
loose	0.95	0.01	0.05
tight	0.95	0.01	0.04
ultra-tight	0.88	0.01	0.05

Table 3.3 – Scale factors for SecVTX modes and relative uncertainties.

3.5.3 The JetProb algorithm

The JetProb algorithm [42] was adopted at CDF in the early days of the top quark discovery to be used along SecVTX with the aim of increasing the b-tagging efficiency. JetProb makes use of the information of the tracks that are associated to a jet to determine the probability for the ensemble of tracks

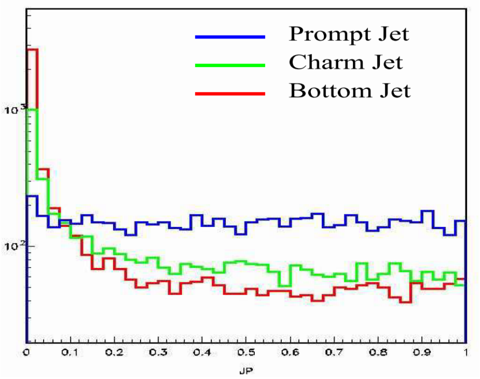

Figure 3.10 – JetProb distribution for prompt, charm and bottom jets.

to be consistent with originating from a primary vertex (*primary jet*).

The JetProb distribution for a jet with no displaced tracks is made by construction uniform from 0 to 1. For a jet containing a displaced component, such as those produced by the decay of a heavy-flavour hadron, the probability distribution is sharply peaked at 0; in other words, the probability for such a jet to originate fully from a primary vertex is very low (fig. 3.10). Unlike SecVTX, JetProb has a continuous output from 0 to 1, so that different working points can be chosen depending on the desired *b*-tagging efficiency and purity.

Chapter 4

Composition and Modeling of the Selected Data Sample

This analysis in centered on the search for $W' \to tb$ production in events where $t \to Wb$ and the W decays leptonically, but the lepton (e or μ) is not identified, or when the τ decays hadronically and is reconstructed as a jet. In order to isolate these events, a series of online and offline selection criteria is applied on both CDF data and simulations, and the resulting distributions are compared to verify the validity of our predictions.

4.1 Data sample and online selection

In this work the full dataset collected by CDF in Run II[1] is analysed. The high-$\not{E}_T$ data stream (emet) is used, accepting a combination of MET_DIJET (p15-p38) and various iterations of MET_35 (p0-p14) trigger paths, for a total integrated luminosity of about 9.1 fb^{-1}. Trigger requirements for MET_DIJET and one MET_35 version are given in table 4.1.

---

[1] Events collected by CDF are individually identified by an *event number* and collected into *runs*, which are then grouped into *periods*. The full CDF II dataset corresponds to periods p0-p38

	MET_DIJET	MET35_&_CJET_&_JET v1
L1	$\not\!\!E_T > 15$ GeV one jet $E_T > 10$ GeV	$\not\!\!E_T > 25$ GeV
L2	$\not\!\!E_T > 28$ GeV two jets $E_T > 3$ GeV $\lvert\eta\rvert < 3.6$	one jet $E_T > 10$ GeV $\lvert\eta\rvert < 1.1$ one jet $E_T > 10$ GeV $\lvert\eta\rvert < 3.6$
L3	$\not\!\!E_T > 30$ GeV	$\not\!\!E_T > 35$ GeV

Table 4.1 – Trigger requirements at the three levels for trigger paths MET_DIJET and MET_35.

4.2 Event preselection

The following *preselection cuts* are applied to events accepted by the online selection.

- $\not\!\!E_T > 50$ GeV

  This cut on L5-corrected $\not\!\!E_T$ is stricter that the conditions imposed by the trigger, and helps rejecting background events in which the $\not\!\!E_T$ is due to instrumental mismeasurements rather than a real neutrino.

- $2 \leq N(\text{jets}) \leq 3$

- $E_T(j_1) > 35$ GeV, $E_T(j_2) > 25$ GeV

  Jets are reconstructed offline using the JETCLU algorithm with a cone in the $\eta - \phi$ space of radius $R = 0.4$. Events with two or three high-p_T jets, ordered with decreasing E_T, are included in the selection; events with a larger number of jets are rejected.

- $|\eta(j_1)| < 0.9$

The leading jet is required to be central to match the trigger requirements.

- $|\eta(j_{1,2})| < 2.0$

  The leading jets are required to be *not forward*.

- $\Delta R(j_1, j_2) > 1$

  It has been observed that the trigger efficiency depends on the distance in R-space between the two leading jets. $\Delta R > 1$ is required to avoid cluster merging at L2, which would result in a loss of efficiency.

- lepton veto: events with one or more isolated leptons are rejected.

  Since we require large missing transverse energy and no leptons, we employ a set of reversed loose lepton identification criteria to ensure that events with true leptons are excluded. To impose track isolation we use a slightly modified version of the commonly used CMIO muon identification [45].
  Lepton rejection is optimized to ensure minimal overlap with the *Lepton plus Jets* sample. The two samples are estimated to be statistically independent to less than 2% of the events.

- $\Delta\phi(\not{E}_T, j_2) > 0.4$.

  A large imbalance in measured transverse energy can be caused by a mismeasurement of the energy of one of the jets in the calorimeter. Thus, in a process in which the $\not{E}_T$ is instrumental rather than due to the presence of a real neutrino in the final state, most of the time the poorly measured jet will be the second highest E_T jet, and the $\not{E}_T$ will be aligned to it in the transverse plane; for this reason angular separation in the transverse plane between the $\not{E}_T$ and the second leading jet j_2 is required. This cut is essential to reject backgrounds in which the $\not{E}_T$ is mainly instrumental such as QCD multijet production.

- $N(b\text{-jets}) \geq 1$

  Since the signal has two real b quarks in the final state, a requirement on the b-tagging of the jets is a straightforward choice to reject background processes with light quarks in the final state.
  The primary b-tagging method is SecVTX in its *tight* implementation; to increase tagging efficiency, SecVTX has been paired with JetProb ($< 5\%$). To allow a more accurate treatment of the b-tagging requirements, the sample has been subdivided into three statistically independent regions according to a corresponding number of exclusive tagging categories. The b-tagging categories are defined as follows (S stands for SecVTX, J for JetProb):

  - 1S: only one of the two leading jets is tagged by SecVTX;
  - SJ: one of the two leading jets is tagged by SecVTX, and the other one is not tagged by SecVTX but by JetProb;
  - SS: both of the leading jets are tagged by SecVTX.

4.3 Signal and background modeling

4.3.1 Signal

Signal samples have been created for eight different values of W' mass (*mass points*), from $M_{W'}$ = 200 GeV to 900 GeV in 100 GeV intervals. W' production is simulated by PYTHIA using the standard W' process, with only the tb decay channel open.
Samples in the range $300 \leq M_{W'} \leq 900$ are normalized to the current best CDF limits [19]. Since a corresponding limit for $M_{W'}$ = 200 GeV does not exist, the sample for $M_{W'}$ = 200 GeV is normalized to the theoretical cross-section [20].

$M_{W'}$ (GeV/c^2)	$\sigma \times \mathcal{B}$ (pb)	2009 CDF limit (obs) (pb)
200	39.43	-
300	44.14	1.59
400	16.65	1.17
500	5.922	0.84
600	2.100	0.44
700	0.743	0.32
800	0.262	0.26
900	0.093	0.26

Table 4.2 – Theoretical cross-section and CDF observed limits for W' mass points considered for this analysis. From [20], [19].

4.3.2 Background processes

In order to correctly model the contribution from SM processes to the various distributions in the selected data sample in both *shape* and *rate* (i.e normalization of the distribution, corresponding to the number of expected events), a combination of Monte Carlo simulations and data-driven methods has been used. Several process can produce signatures consistent with large $\not\!\!E_T$, two or three high-p_T jets and b-tagging requirements. They are grouped in the following templates: a short description of each process and of the techniques used to model them is given.

$t\bar{t}$ Pair production of top-antitop quarks occurs at Tevatron mainly via $q\bar{q}$ (85%) or gg (15%) interactions. $t\bar{t}$ events have up to two high-p_T leptons and a variable number of high-p_T jets in the final state, depending on the decay modes of the W bosons. Due to the presence of W bosons and real b quarks in the final state, this process is an important source of background in the selected sample, especially in the SS and SJ tagging categories where two b-tagged jets are required.

The $t\bar{t}$ sample is simulated by PYTHIA assuming a value for the top mass

$m_{\text{top}} = 172.5$ GeV. For the normalization of the $t\bar{t}$ sample the measured CDF cross section of 7.71 ± 0.51 pb [47] is used.

Diboson This process includes the associated production of pairs of vector bosons (WW, WZ, ZZ). Diboson contribution to a b-tagged sample is due both to real heavy-flavour quarks in the final state ($Z \to b\bar{b},\ c\bar{c},\ W \to cs$) and light-flavour contamination (mistags).
Diboson production is simulated using LO PYTHIA. A corrective factor k_{NLO} corresponding to the ratio between NLO and LO cross-section estimate in MFCM is applied to the predicted rate.

Single top Single top EW production at Tevatron occurs mainly via t-channel and s-channel processes. The topology of final state is very similar for $W' \to tb$ and LO single top s-channel; indeed, $W' \to tb$ can be thought of as the same process in which the time-like virtual W boson is replaced with a on-shell W'. These properties have been exploited in the training of the multivariate tool used to reject the QCD multijet background (see chapter 5).
Single top production is simulated via PowHeg. The rate predicted by the Monte Carlo is in good agreement with experimental results and is used to normalize the sample.

***W*/*Z* + jets** This template includes associated production of W or Z bosons with high-p_T jets. The contribution to the b-tagged selected sample is due to both real heavy-flavour ($Z \to b\bar{b},\ c\bar{c},\ W \to cs$, QCD production of real b-jets) and light-flavour contamination (mistags). W/Z + jets is simulated using ALPGEN + PYTHIA. The theoretical cross section of W/Z + jets is only known to the lowest order in QCD and suffers from large uncertainties. For this reason, only the shape of the distribution is well-modeled, while a data-driven method is used to derive the normalization for each tagging

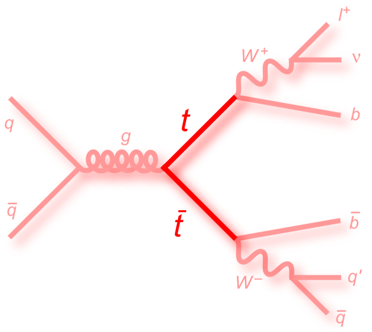

Figure 4.1 – Feynman diagram for a semileptonic $t\bar{t}$ event.

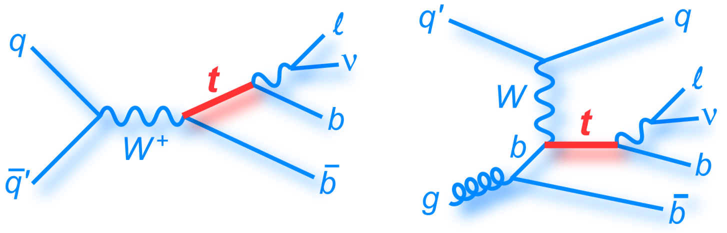

Figure 4.2 – Feynman diagrams for single top s-channel (left) and t-channel (right).

category.

QCD multijet In QCD multijet production, high-p_T jets are generated as a result of Quantum Chromo-Dynamics interactions. QCD multijet production has a large cross-section (several μb), which is about 6 orders of magnitude larger than the signal if no b-tag requirements are applied.
In most cases, the $\not{E}_T$ is due to mismeasurements of the jet energy; semileptonic decays of heavy-flavour hadrons can also contribute if the lepton isn't correctly identified. Due to the large cross-sections, it is practically impossible to generate enough events to simulate all QCD processes. For this reason, a method for estimating QCD background from data was developed at CDF [44]. This technique is based on a data-driven Tag Rate Matrix to estimate contribution from both real heavy-flavor QCD production and events with a light-flavor jet falsely tagged as a b quark (mistags).

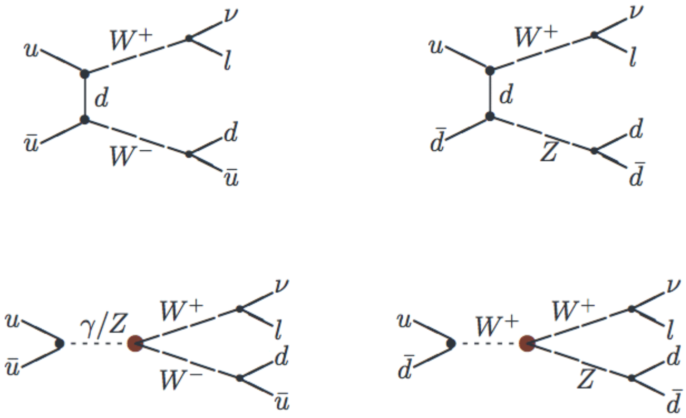

Figure 4.3 – Feynman diagrams for WW and WZ production.

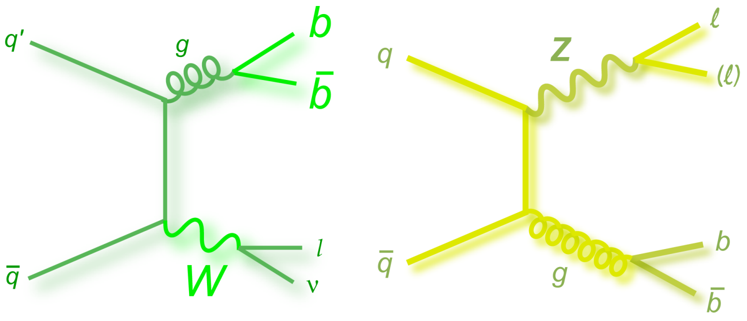

Figure 4.4 – Examples of Feynman diagrams for $Wb\bar{b}$ (left) and $Zb\bar{b}$ (right) production decaying to finals states accepted by our selection criteria.

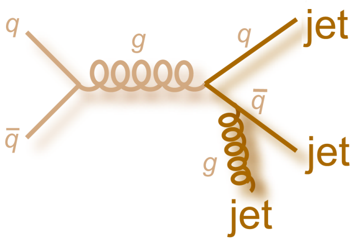

Figure 4.5 – Feynman diagram for one of the many QCD multijet production processes.

Process	Modeling	Cross Section (pb)
QCD multijet	data-driven	data-driven
W/Z + jets	ALPGEN + PYTHIA	data-driven
$t\bar{t}$	PYTHIA	7.71 ± 0.51 (measured)
single top s-channel	PowHeg	1.05 ± 0.17
single top t-channel	PowHeg	2.12 ± 0.32
WW	PYTHIA	12.4 ± 1.4
WZ	PYTHIA	3.7 ± 0.4
ZZ	PYTHIA	3.6 ± 0.4

Table 4.3 – A summary of SM background processes, and the method used for their modeling.

QCD multijet	12338.1 ± 866.5	984.9 ± 69.9	426.6 ± 31.5
V + jets	4434.2 ± 232.9	244.1 ± 20.8	56.6 ± 4.4
diboson	226.2 ± 27.1	23.4 ± 3.2	24.9 ± 3.2
$t\bar{t}$	965.2 ± 85.6	185.0 ± 20.1	202.5 ± 20.7
single top	311.2 ± 29.7	47.4 ± 5.3	56.0 ± 6.1
Expected	18436.7 ± 902.3	1541.4 ± 76.1	840.5 ± 38.9
Observed	18494	1448	807
($M_{W'}$ = 300 GeV)	161.9 ± 8.5	56.6 ± 4.8	73.9 ± 5.5

Table 4.4 – Event yields in preselection region. The template for W' = 300 GeV is superimposed to the background distribution for comparison.

4.4 Modeling in the preselection region

The total number of expected and observed events is given in table 4.4. In order to further validate our predictions, we check the agreement between the data and the predictions in several distributions. The corresponding plots are shown in the following pages.

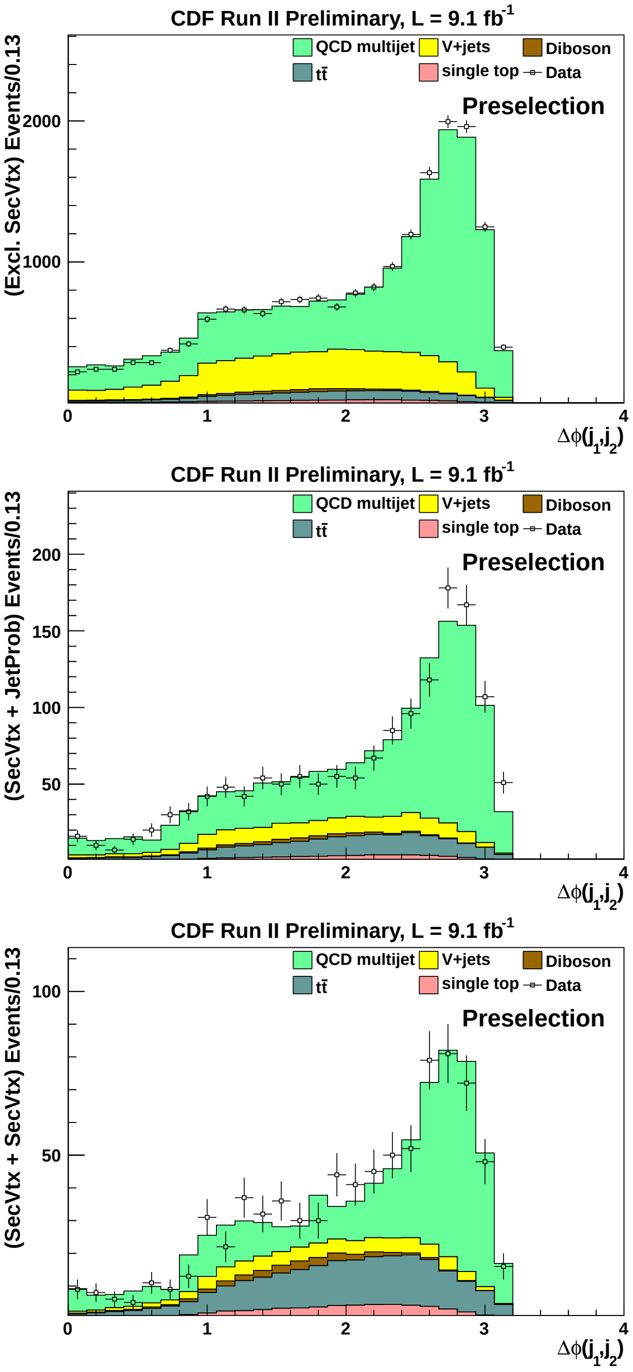

Figure 4.6 – Difference in ϕ between missing transverse energy $\not{E}_T$ and missing transverse momentum $\not{p}_T$ in preselection region. From top: 1S, SJ, SS.

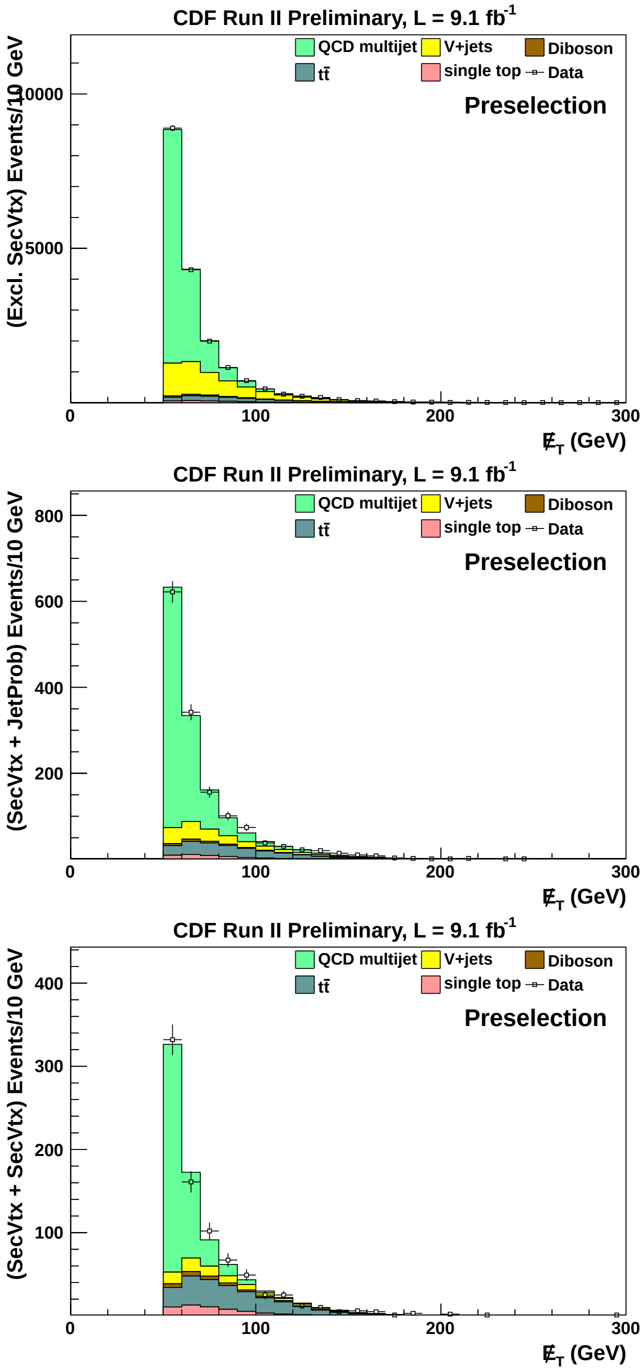

Figure 4.7 – Missing transverse energy. From top: 1S, SJ, SS.

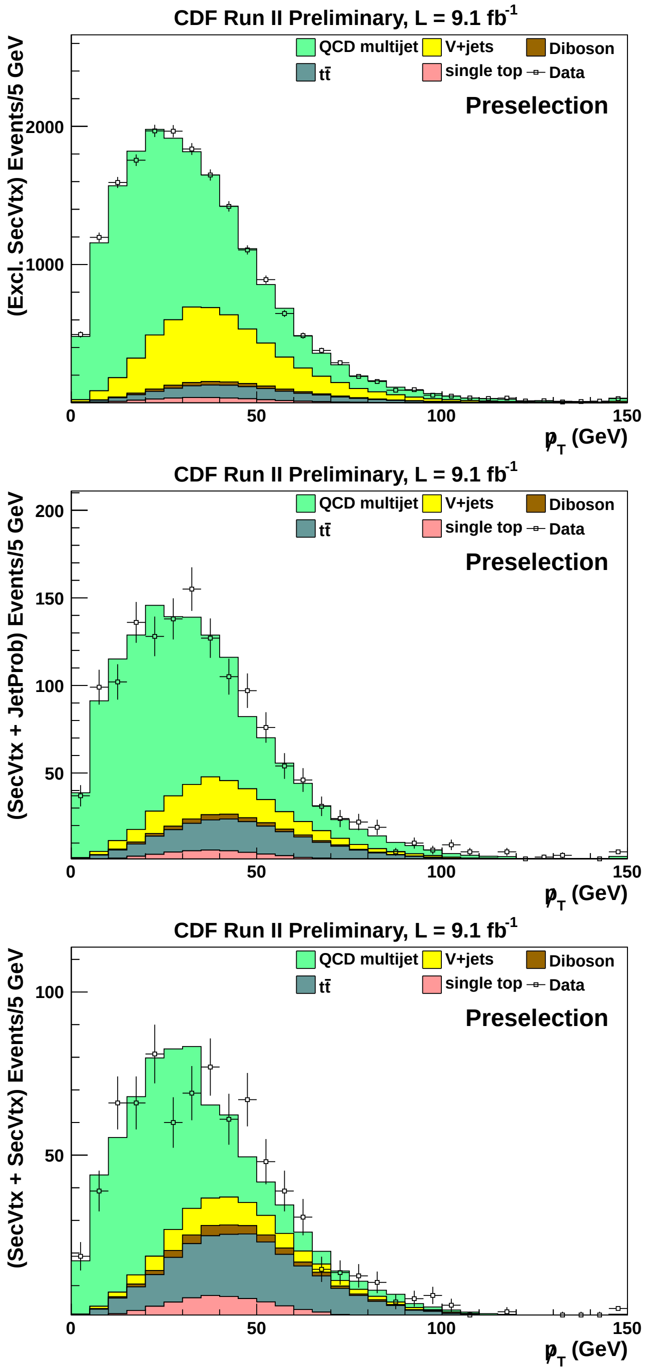

Figure 4.8 – Missing transverse momentum. From top: 1S, SJ, SS.

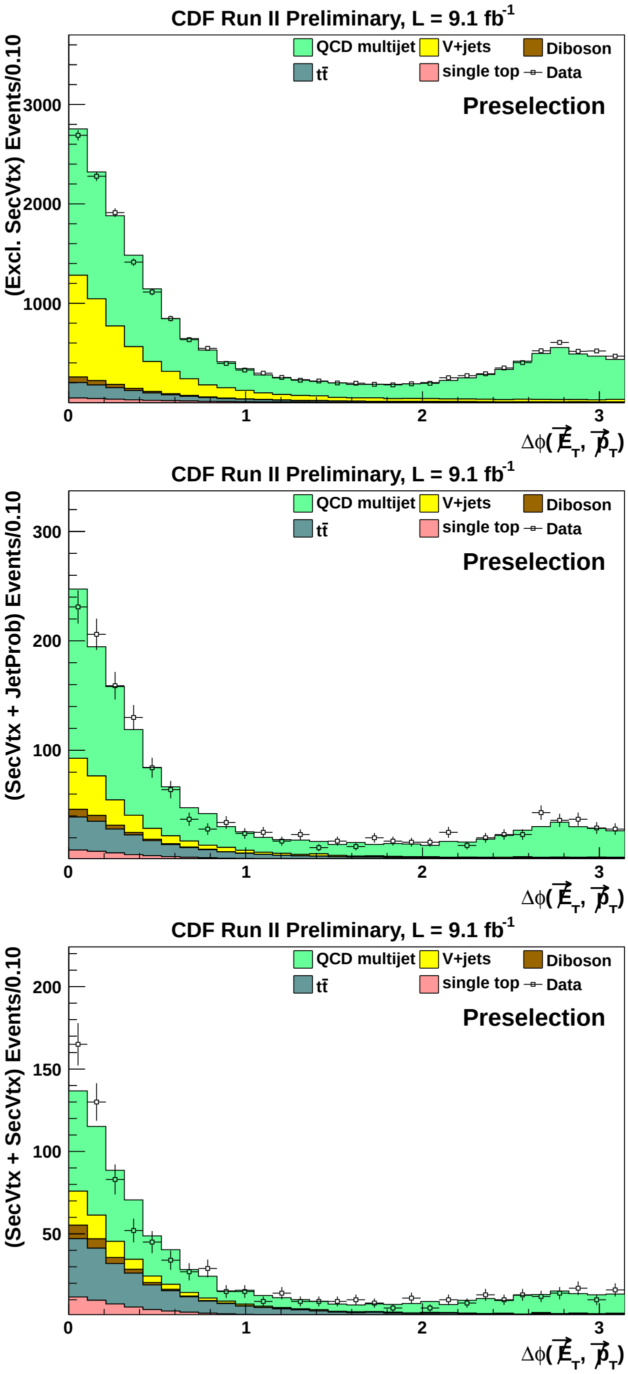

Figure 4.9 – Distance in ϕ between $\vec{\not\!\!E}_T$ and $\vec{\not\!p}_T$. From top: 1S, SJ, SS.

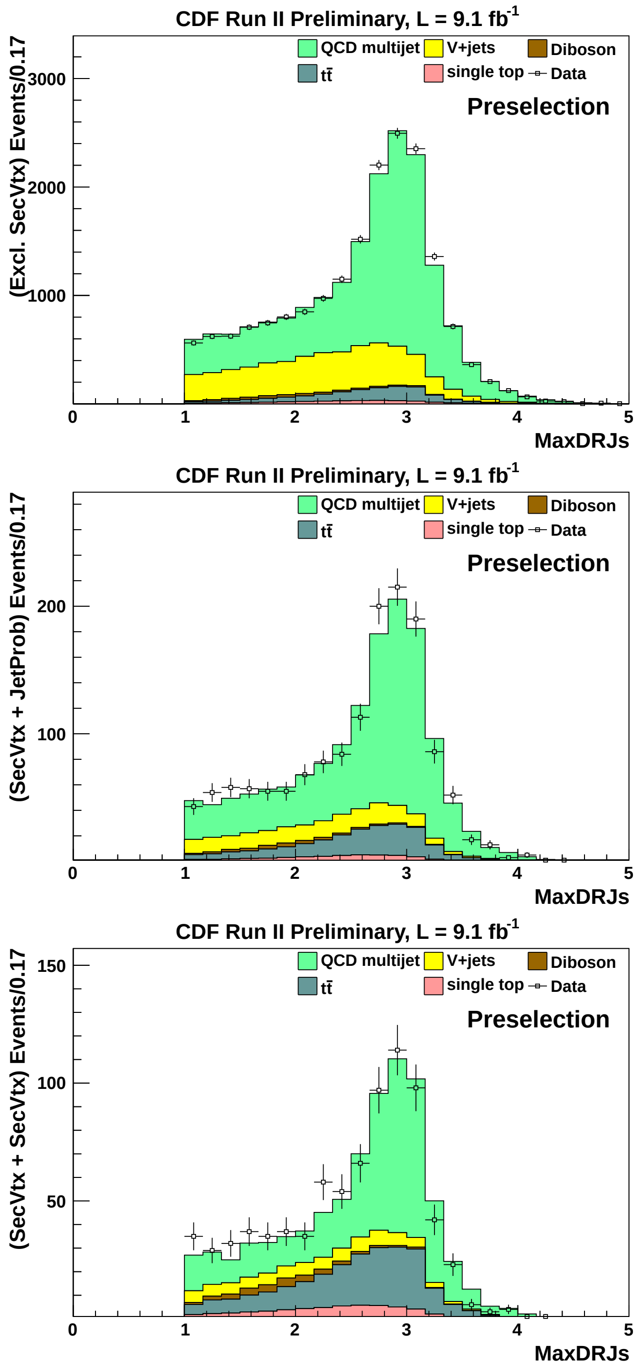

Figure 4.10 – Maximum distance in R-space between jets. From top: 1S, SJ, SS.

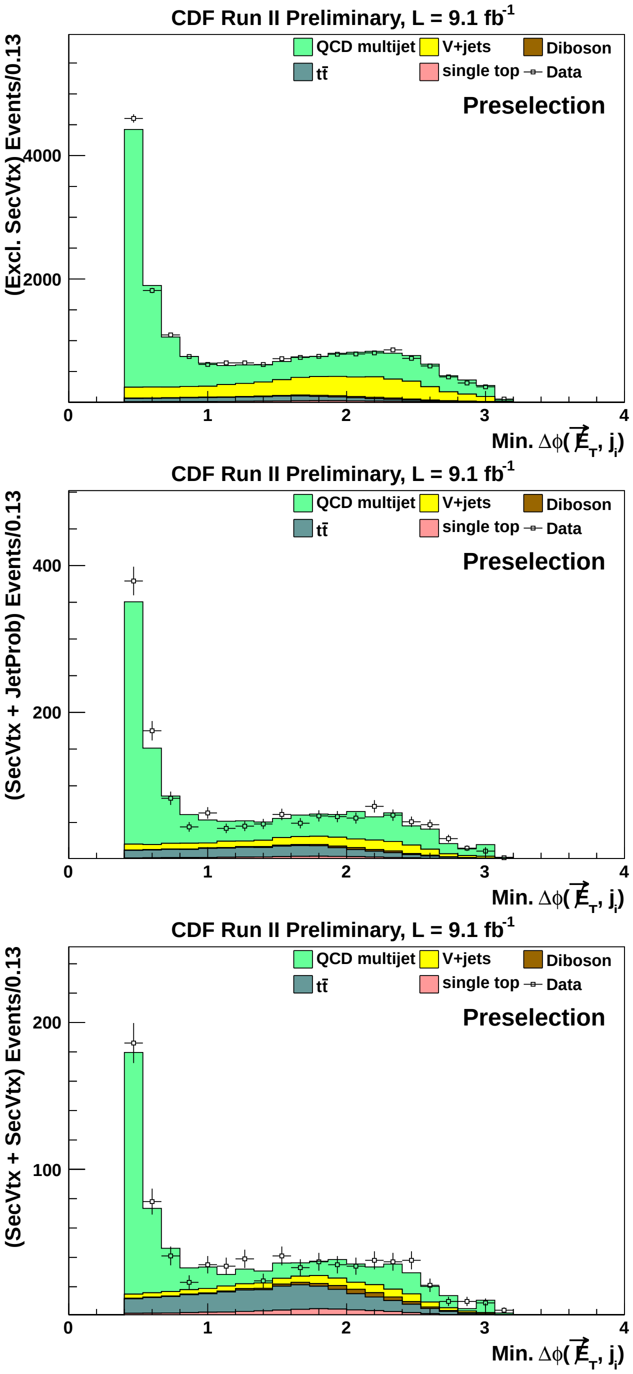

Figure 4.11 – Minimum distance in ϕ between $\vec{\not\!\!E}_T$ and jets. From top: 1S, SJ, SS.

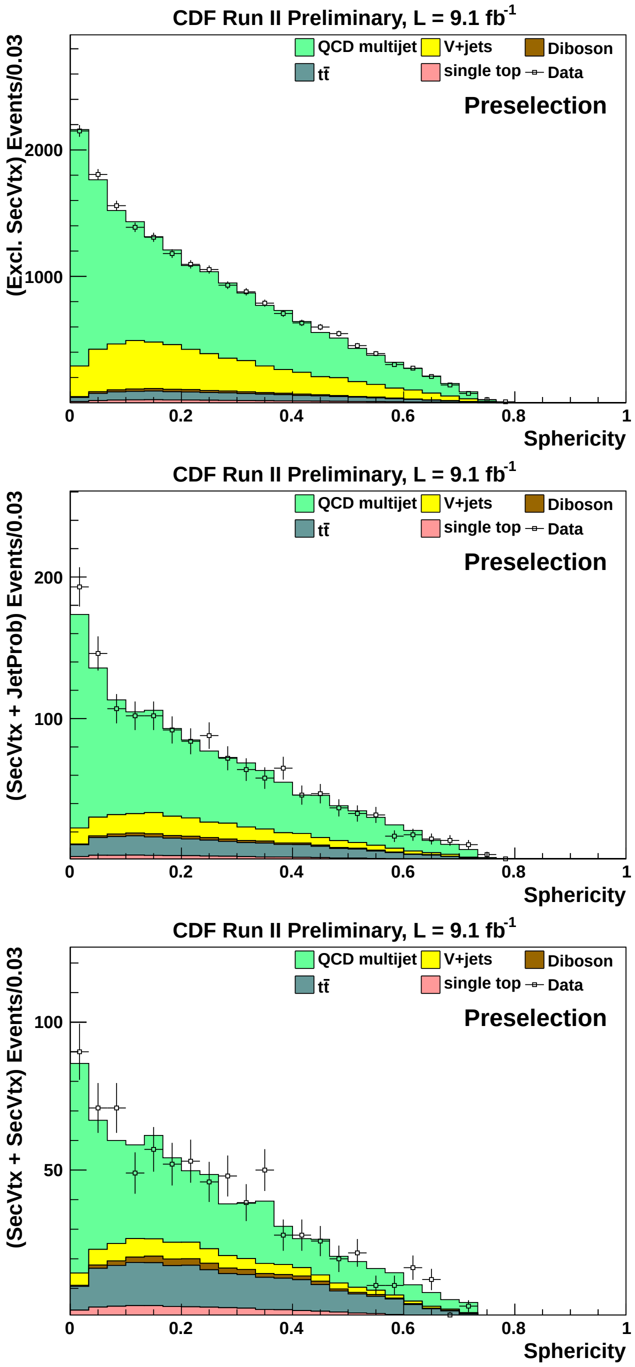

Figure 4.12 – Sphericity. From top: 1S, SJ, SS.

4.5 Control regions

Control regions are defined reversing one or more selection cuts. By definition, control regions are orthogonal to the preselected sample, and provide statistically independent events, for model testing or for deriving useful quantities such as scale factors.

In this analysis, the following control regions are used:

- `TRM` region: $\Delta\phi(\not{E}_T, j_2) < 0.4$, $50 < \not{E}_T < 70$

  Reversing the cut on $\Delta\phi(\not{E}_T, j_2)$ defines a QCD-enriched region. Events in the `TRM` region are used to derive the data-driven template for QCD multijet [44].

- `QCD` region: $\Delta\phi(\not{E}_T, j_2) < 0.4$, $\not{E}_T > 70$

  The `QCD` region is used to validate the QCD template.

- `EWK` region: $\Delta\phi(\not{E}_T, j_2) > 0.4$, $N(\text{lepton}) \geq 1$

  This region is defined by reversing the veto on the presence of identified leptons. It it used for validation of the modeling.

A scheme of the control regions is shown in fig. 4.13.

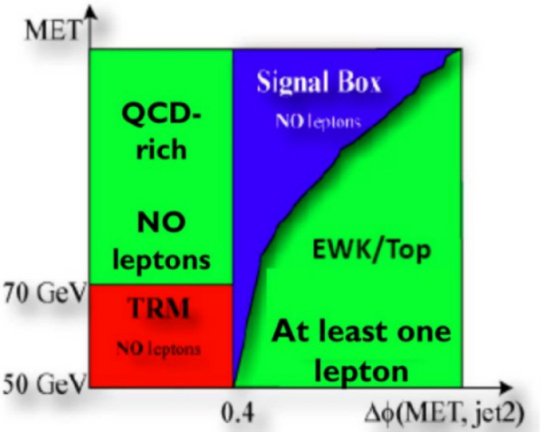

Figure 4.13 – Scheme of the control regions.

Chapter 5

QCD multijet background rejection

As can be seen from table table 4.4, QCD multijet production is by far the largest contributor to the selected sample. Thus, we first develop a method based on a multivariate object to reduce the QCD multijet contribution and define a *signal region*.

Then, from events in the signal region we choose a distribution, known as *final discriminant*, on which we perform the statistical analysis comparing the expected distribution and the data.
For this analysis, the variable chosen as final discriminant is the transverse invariant mass of the $\not{E}_T$ and all the jets in the final state, denoted as $M_T(\not{E}_T, j_{1,2,3})$.

5.1 QCDNN

To reduce QCD background, applying further orthogonal cuts, such as those used to define the preselection region, is not a viable strategy since it would lead to losing a large fraction of the signal as well. Furthermore, orthogonal cuts are unable to take into account the correlations existing among the many variables in which QCD multijet differs from other background processes and from the signal.

For this reason, a MultiVariate Analysis (MVA) approach is the optimal choice. For this analysis, we have developed a tool, named `QCDNN`, based on a Artificial Neural Network (ANN). A detailed description of its design and performance is given in the following.

5.1.1 Architecture

An ANN receives in input a series of variables, and then internally processes them so as to exploit the correlations between them. The resulting output is a distribution in which the signal and the background are separated.

`QCDNN` is a MultiLayer Perceptron (MLP), a common type of ANN. It is a simple feed-forward network: signals flow from the input units, or *neurons*, via links, or *synapses*, through one or more hidden units, logically grouped into *layers*, eventually reaching the output neurons. Each neuron computes the output of the previous layer according to a linear combination of the neuron's *activation functions*. The synapses store parameters, called weights, that manipulate the data in the calculation.

For `QCDNN`, an architecture with a sigmoid transfer function and one hidden layer with $N + 5$ neurons is chosen.

5.1.2 Input variables to QCDNN

A total of $N = 13$ input variables are used. These are:

- missing transverse momentum, $\not{p}_T$
- missing transverse energy, $\not{E}_T$

- difference in ϕ between missing transverse energy $\not{E}_T$ and missing transverse momentum $\not{p}_T$, $\Delta\phi(\not{E}_T, \not{p}_T)$
- maximum difference in R-space between two jets, for all jet pairs
- minimum difference in ϕ between the $\not{E}_T$ and each jet
- minimum difference in ϕ between the $\not{p}_T$ and the jets, considering all $(\not{p}_T, j_i)$ pairings
- maximum difference in ϕ between jet directions, for all jet pairs;
- ratio of H_T, vector sum of *tight* jet E_T, over $\not{E}_T$
- $\Delta\phi$ between the direction of the leading jets in the jet pair rest frame and the direction of the jet pair boost
- metsig, the ratio between $\not{E}_T$ and the square root of the summed E_T over all calorimetric activity
- Event sphericity $S = 1.5 \times (\lambda_2 + \lambda_3)$, where the λ_i are the eigenvalues of the sphericity tensor[1].
- invariant mass of $\not{E}_T$, j_1 and j_2

5.1.3 Training

In the training of a NN, the choice of the training samples is extremely important to ensure a good separation between signal and background and a consistent behaviour of the tool.

The background sample is composed of QCD multijet events that pass the preselection cuts, modeled with the data-driven method described in section 4.3.2.

---

[1] For N particles, if p_i is the momentum of the ith particle, the sphericity tensor is defined as $M_{\alpha\beta} = \sum_{i=1}^{N} p_{i\alpha} p_{i\beta}$, $(\alpha, \beta = x, y, z)$.

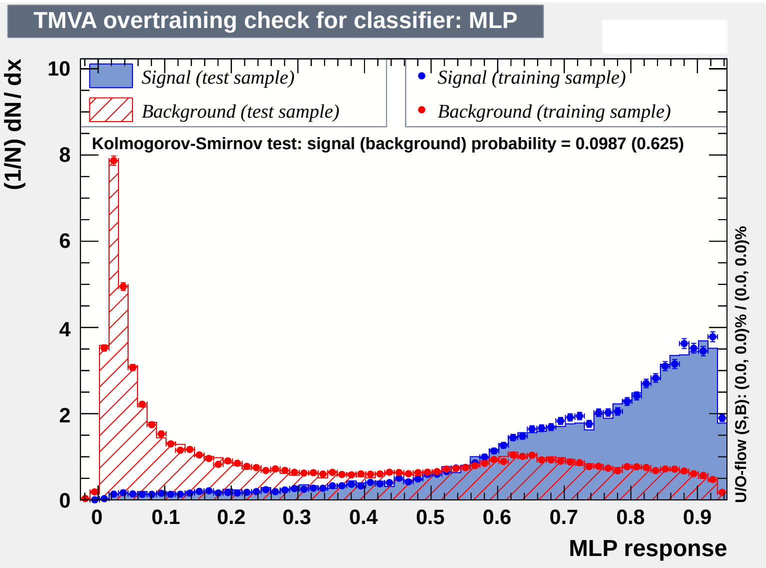

Figure 5.1 – KS test for the training of `QCDNN`. The two distributions for the signal and background samples are shown.

For the signal sample, single top s-channel events are used. With the exception of the different boson mass, W' and single top events share the same final state. Their kinematics will be very similar. Therefore, the same QCD rejection performance will be ensured across the whole $M_{W'}$ range without having to develop a separate tool for each W' mass point, since kinematical distributions for the single top s-channel training sample do not contain, by definition, information about $M_{W'}$.

Properties related to the resonant behaviour of the invariant mass distributions of W' decay products are exploited later in the analysis, since $M_T(\not{E}_T, j_{1,2,3})$ is chosen to be the discriminating variable for the final fit.

To check for the presence of *overtraining* [46], both background and signal samples are divided in two statistically independent *test* and *training* subsamples, and a Kolmogorov-Smirnov (KS) validity test is performed. Figure 5.1 shows an excellent agreement between the subsamples, indicating that no overtraining has occurred.

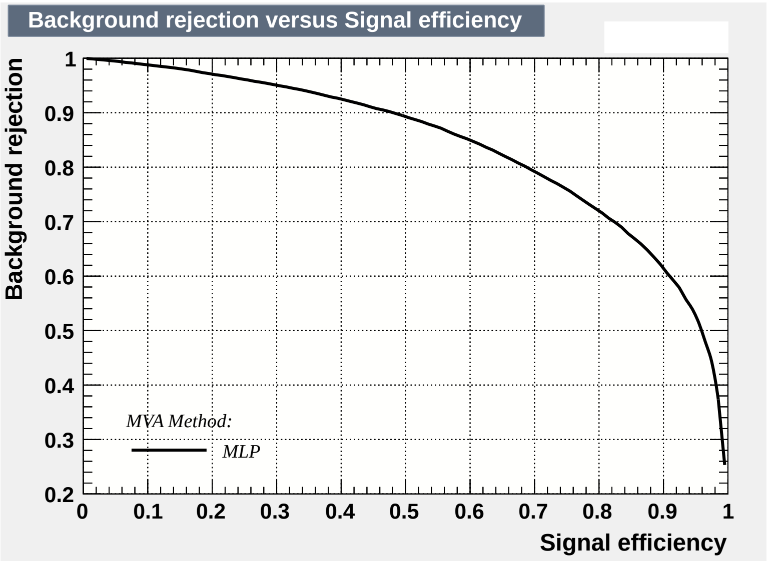

Figure 5.2 – ROC curve for QCDNN.

5.1.4 QCDNN output

After the training procedure, QCDNN is implemented into the analysis framework and applied to the preselected sample. The distribution of the output of QCDNN, denoted as qcdnn, is shown in figures section 5.1.4 and fig. 5.4.

ROC curve One way of measuring the performance of a signal/background classifier is through its ROC curve. The ROC curve is created by plotting the background rejection factor, i.e. the fraction of the amount of background events that pass the selection, as a function of signal efficiency, i.e. the amount of signal events that pass the selection, for different values of the selection threshold. Figure 5.2 shows the Receiver Operating Characteristic (ROC) curve for QCDNN.

The cuts on the QCDNN output define three independent regions.
The signal region S is defined by the interval qcdnn $> \alpha$. After optimization studies, we choose $\alpha = 0.45$. This choice allows a rejection factor for QCD

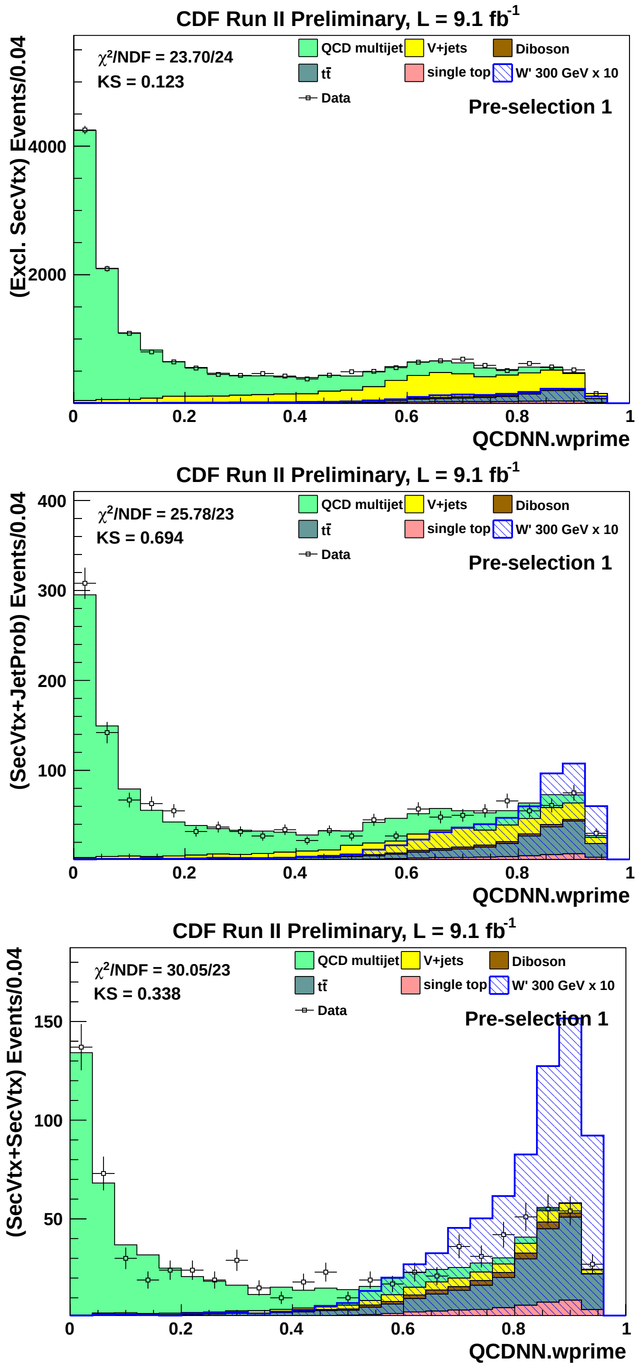

Figure 5.3 – QCDNN distribution in preselecion region. The template for W' = 300 GeV ($\times$10) is superimposed for comparison. From top: 1S, SJ, SS.

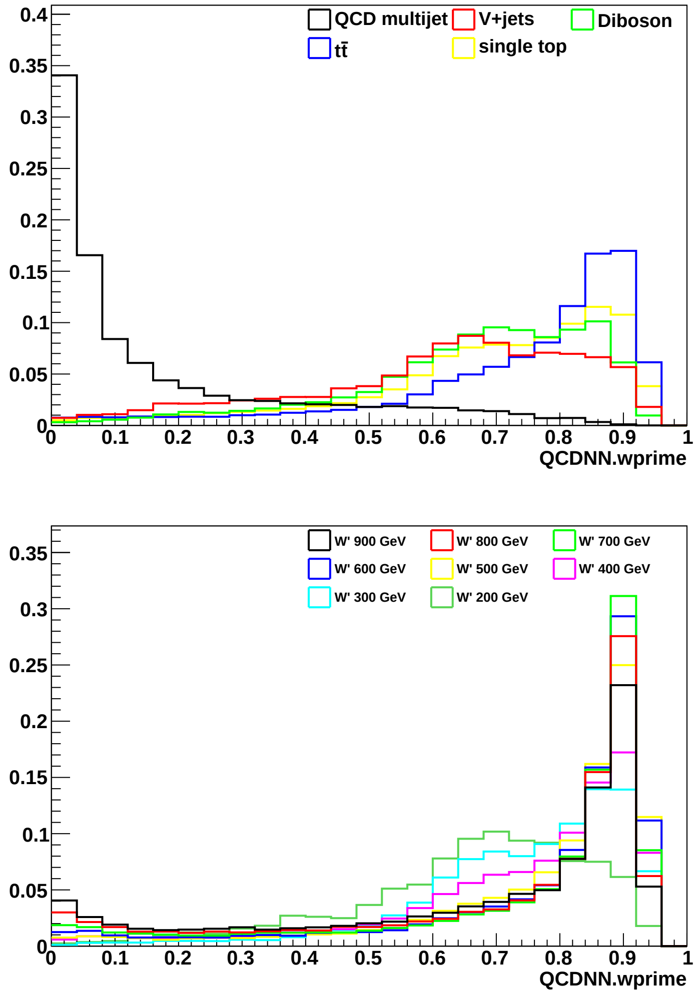

Figure 5.4 – qcdnn distribution comparison for background (top) and signal templates (bottom), normalized to unity. A good separation from the QCD multijet background is shown in both cases, validating the assumptions on the choice of the training samples.

multijet of $\sim 65\%$ and a signal efficiency of $\sim 90\%$.

The intervals $0 \leq \texttt{qcdnn} < 0.1$ and $0.1 \leq \texttt{qcdnn} < 0.3$ define respectively the control regions A and B, that are used to estimate the pre-fit value for QCD multijet and V + jets rate.

Prefit estimate for QCD and V + jets rate As seen in section 4.3.2, due to the uncertainties in the Tag-Rate Matrix used to derive our predictions for both QCD and V + jets background, these processes suffer from poorly predicted rates. The modeling in the preselection and the signal region would be unsatisfactory if the uncorrected normalizations are used.

A novel data-driven approach to calculate the normalization of both QCD multijet and V + jets has been developed for this analysis.

The procedure is as follows. Region A, defined as $0 \leq \texttt{qcdnn} < 0.1$, is QCD-dominated. A scale factor k_A is derived for QCD multijet by subtracting Monte Carlo predictions (signal, EW processes, $t\bar{t}$, V + jets MC estimate) from the number of observed events:

$$k_A = k_{\text{QCD}} = \frac{N_A(\text{data}) - \sum_i N_A^i(\text{MC}_i)}{N_A(\text{QCD})}. \tag{5.1}$$

Region B, defined as $0.1 \leq \texttt{qcdnn} < 0.3$, is QCD multijet- and V + jets-dominated, in a relative proportion which is close to the proportion in the whole preselection region. A scale factor k_B is derived for a template that comprises both QCD multijet and V + jets by subtracting Monte Carlo predictions (signal, EW processes, $t\bar{t}$) from the number of observed events:

$$k_B = \frac{N_B(\text{data}) - \sum_i N_A^i(\text{MC}_i)}{N_B(\text{QCD} + \text{VJ})}. \tag{5.2}$$

To obtain the scale factor k_{VJ} for the V + jets rate, the corrected QCD contribution is subtracted from the corrected number of QCD plus V + jets events in the whole preselection region P, and the result is divided for the uncorrected expected V + jets yield:

$$k_{\mathrm{VJ}} = \frac{k_B \cdot N_P(\mathrm{QCD} + \mathrm{VJ}) - k_{\mathrm{QCD}} \cdot N_P(\mathrm{QCD})}{N_P(\mathrm{VJ})} \tag{5.3}$$

The procedure is performed separately in each of the *b*-tagging regions 1S, SJ, SS so as to obtain a specific scale factor for each tagging category.

This technique also allows for a more stringent estimate on the uncertainty on QCD normalization in the signal region, which is calculated via the uncertainty δk_{QCD} on the scale factor k_{QCD}:

$$\frac{\delta k_{\mathrm{QCD}}}{k_{\mathrm{QCD}}} = \sqrt{\left(\sum_i \frac{\sqrt{\delta \mathrm{MC}_i^2(stat) + \delta \mathrm{MC}_i^2(syst)}}{\mathrm{data} - \mathrm{MC}_i} \right)^2 - \left(\frac{\delta N_A(\mathrm{QCD})}{N_A(\mathrm{QCD})} \right)^2}, \tag{5.4}$$

where the sum is taken on the Monte Carlo processes considered in eq. (5.1).

5.2 Modeling in the signal region

The total number of expected and observed events is given in table 5.1.

The $M_T(\not{E}_T, j_{1,2,3})$ distribution, in the three tagging categories is shown in section 5.2. The distribution shows no excess above SM predictions; thus, in chapter 6, we will estimate upper limits on $\sigma(p\bar{p} \to W') \times \mathcal{B}(W' \to tb)$.

QCD multijet	1756.8 ± 130.3	225.6 ± 17.5	60.5 ± 6.5
V + jets	3458.8 ± 182.0	199.8 ± 17.2	47.3 ± 3.6
diboson	218.3 ± 26.2	28.1 ± 3.9	23.5 ± 3.0
$t\bar{t}$	831.7 ± 73.8	193.9 ± 21.1	191.5 ± 19.5
single top	263.7 ± 25.2	49.7 ± 5.6	52.6 ± 5.7
Expected	6681.9 ± 238.7	751.2 ± 33.4	447.0 ± 22.5
Observed	6815	620	405
($M_{W'}$ = 300 GeV)	152.7 ± 8.1	54.1 ± 4.5	71.6 ± 5.4

Table 5.1 – Event yields in signal region.

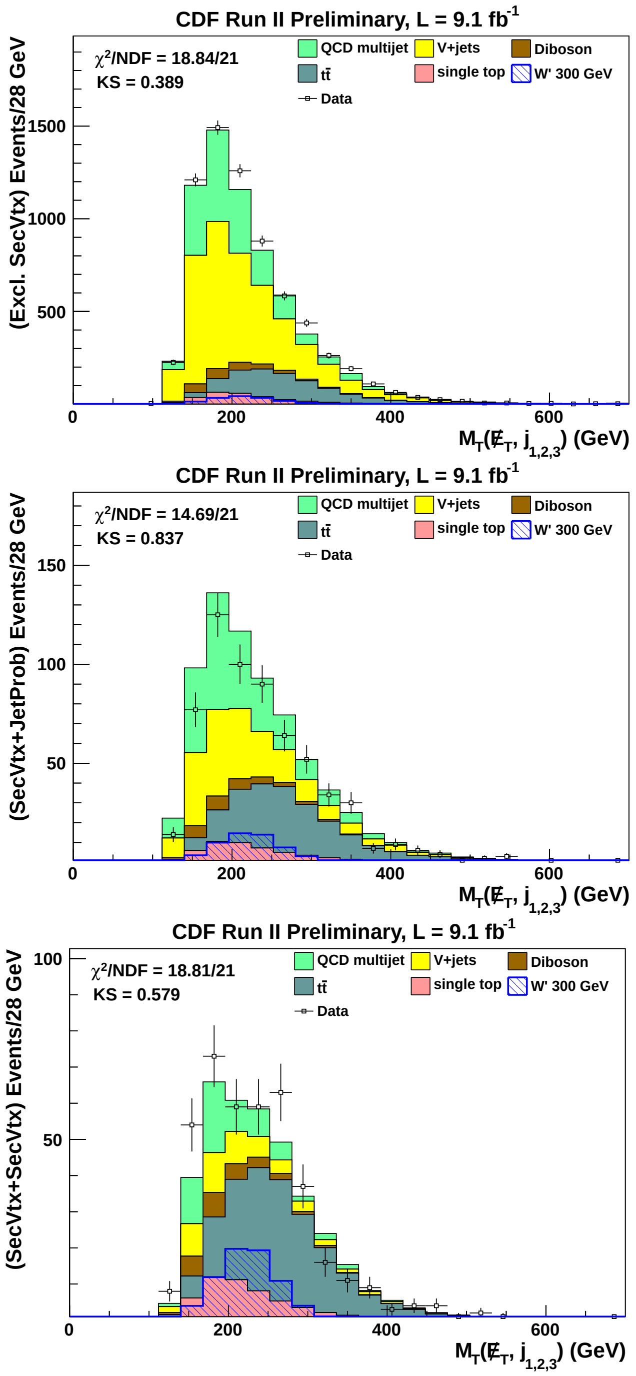

Figure 5.5 – $M_T(\not{E}_T, j_{1,2,3})$ distribution in signal region. From top: 1S, SJ, SS. The template for $W' = 300$ GeV is superimposed to the background distribution for comparison. From top: 1S, SJ, SS.

Chapter 6

Setting the Limits

As seen in previous chapter, the observed $M_T(\not{E}_T, j_{1,2,3})$ distribution shows no significant excess above SM predictions. Therefore, we place upper limits on the production of W' decaying to a top and a bottom quark. In order to calculate the upper limits, we analyze the $M_T(\not{E}_T, j_{1,2,3})$ distribution with a binned maximum-likelihood fit. The limits are computed using the Bayesian likelihood method with flat prior probability for the signal cross section, and Gaussian priors for the uncertainties on acceptance and backgrounds. The software package we use for limit computation is called mclimit [53] and contains an implementation of a multichannel Bayesian limit calculator capable of taking into account the correlations between various acceptance and background priors.

6.1 Bayesian approach

In the simplest case of a counting experiment and a single source of background, the Bayesian approach to calculate the limit is the following.

Let us assume an experiment is performed, and n events (Poisson distributed) are observed, with a mean expectation $s\epsilon + b$, where s is the number of expected signal events, ϵ is an overall acceptance factor (including

branching fraction, detector efficiency, analysis accpetance factor, etc.) and b is the number of expected background events. We now assume that the background is known with arbitrary precision, and the signal acceptance is known (with a precision σ_ϵ) from other measurements.
The Bayes theorem then states that the posterior $p(s, \epsilon|n)$ for s is

$$p(s, \epsilon|n) = \frac{P(n, s|\epsilon)\pi(s)\pi(\epsilon)}{\int\int P(n, s|\epsilon)\pi(s)\pi(\epsilon)\, ds d\epsilon}, \tag{6.1}$$

where $P(n, s|\epsilon)$ is the probability of observing n events in presence of a signal s with acceptance ϵ, while $\pi(s)$ and $\pi(\epsilon)$ are respectively the prior probability densities for s and ϵ. Since the number of observed events in data is Poisson distributed, we have

$$p(n, s|\epsilon) = \frac{(s\epsilon + b)^n}{n!} e^{-(s\epsilon+b)}. \tag{6.2}$$

From eq. (6.2) we can obtain the posterior for s by integration over ϵ:

$$p(s|n) = \int_0^\infty p(s, \epsilon|n) d\epsilon. \tag{6.3}$$

Finally, to obtain the limit on s, the posterior density function $p(s|n)$ is integrated until the desired confidence level (C.L.) is reached. For instance, the 95% C.L. upper limit s_u can be computed from the equation

$$\int_0^{s_u} p(s|n) ds = 0.95. \tag{6.4}$$

6.2 Multichannel Bayesian fit procedure

The method described above refers to a single counting experiment. In the case of a binned distribution of a discriminant variable, with a total number of bins N, we can treat each bin as a statistically independent counting search. Therefore, for the k^{th} bin we will have n_k observed events and

$s\epsilon_k + b_k$ expected events, where s is the total number of expected signal events, while ϵ_k and b_k are the signal acceptance and the amount of expected background in the k^{th} bin. All of the ϵ_k and b_k have uncertainties and are considered *nuisance parameters*; similar to the procedure above, they are assigned priors, that may be correlated (for example, as in the case of luminosity uncertainty). We can write the overall prior as:

$$\pi(\epsilon_1, b_1, ..., \epsilon_n, b_n) \tag{6.5}$$

so that the posterior can be written, as a function of s, according to

$$p(s|n) = \pi(s) \int_{...2N...} \int \pi(\epsilon_1, b_1, ..., \epsilon_n, b_n) \left[\prod_{k=1}^{N} \frac{e^{-(s\epsilon_k + b_k)} (s\epsilon_k + b_k)^{n_k}}{n_k!} \right] d\epsilon_1 db_1 ... d\epsilon_N db_N \tag{6.6}$$

The above integral is calculated with Monte Carlo integration, i.e. generating M random $(\epsilon_1, b_1, ..., \epsilon_n, b_n)$ vectors (*ensemble*) according to their priors, and then averaging over M. The software we used takes into account the correlations between nuisance parameters when generating the random vectors. In this analysis, we use a flat prior for the signal cross-section, and integrate over Gaussian priors for the systematic uncertainties.

We distinguish between *rate* and *shape* uncertainties. Rate systematics are uncertainties on the expected number of signal or background events. Shape systematics arise when systematic effects introduce a significant variation in the distribution of interest (in our case, the $M_T(\not{E}_T, j_{1,2,3})$ distribution). In this case, the random sets are generated while interpolating the histograms within their shape uncertainties. Shape uncertainties are provided as inputs to the mclimit package in addition to the nominal histogram shapes.

6.3 Systematic uncertainties

Systematic uncertainties, or simply *systematics*, are uncertainties that cannot be reduced simply increasing the sample size. They arise from incomplete knowledge of detector effects, like mechanical misalignement, miscalibration or detector noise, or from limited theoretical knowledge of a process in exam. Some categories of systematics, such as the luminosity uncertainties, are the same for all the processes; some others, such as cross sections uncertainties, affects each process in a different amount; finally, some theoretical uncertainties are typical of a single process only.
A detailed list of the systematics considered for this analysis is given below.

Cross Section Uncertainty Since rate is predicted in a different way for each processes, a specific rate systematics is applied for every template

- single top: the normalization is restricted to its predicted cross section within a 15% uncertainty.

- diboson: the normalization is restricted to its predicted cross section within a 6% uncertainty.

- $t\bar{t}$: since $t\bar{t}$ is normalized to the measured cross-section (7.71 ± 0.51 pb [47]), a 6.6% uncertainty is applied to top-antitop production rate.

- V + jets: W + jets background rates are allowed to float unconstrained in each tagging category. Thus, no rate systematics is applied to V + jets production.

- QCD: the method to derive the normalization uncertainty for this template is described in section 5.1.4. The resulting uncertainties are: 1S: 1%; SJ: 6%; SS: 7%.

Luminosity Uncertainty The procedure for determining the uncertainty on the luminosity is described in [48]. This uncertainty amounts to 6% and applies to those simulations that are normalized to luminosity.
This uncertainty does not apply to QCD and V + jets, which are data-driven, and $t\bar{t}$, because the measured cross section is used.

PDF Uncertainty The PDF uncertainty has been determined using the method that is described in [49]. It has been determined [50] that a 2% uncertainty on the acceptance due to the choice of the PDF is sufficient.

Jet Energy Scale Uncertainty The Jet Energy Scale uncertainty was determined by varying the jet energy correction factor by $\pm 1\sigma$. This variation then propagates to the $\not{E}_T$ reconstruction, the calculation of the direction of $\not{E}_T$ and thus to the expected number of events after applying the selection cuts. The influence of this variation is different for each background component; therefore, it must be determined separately by running the entire analysis code twice more on all the simulated backgrounds.
The JES uncertainty can also modify the shape of the distributions.
In some cases, the JES can be very asymmetric. In the cross section calculation the $\pm 1\sigma$ shapes and rates are obtained for backgrounds and signal, thus taking the asymmetric nature of the uncertainty into account.

Renormalization and factorization scales in the W + jets MC (Q^2) The `ALPGEN` event generator used for W + jets events requires renormalization and factorization scales of the Q^2 parameter to be chosen appropriately to account for the finite order perturbative calculations of cross sections and for the factorization approximation of structure functions and cross sections. Since the Q^2 values are not known, and indeed not physically measurable since they are an artifact of the theoretical approximation, an uncertainty is assigned to cover a variety of different possibilities. As a default, the renormalization and factorization scales are set to be the same at $Q^2 = M_W^2 + \Sigma p_T^2$, where M_W is the W boson mass and p_T^2 is the square of the parton transverse momentum. The sum extends over all final state partons [52]. This parameter is doubled and then halved to create two samples which are used to determine the shape uncertainty on the W + jets template. This method addresses the shape uncertainty only.

B-tagging scale factor The efficiency of tagging a taggable jet in the simulation is different from that in real events. This difference has to be taken into account when calculating the predicted number of events in the simulation after requiring a tag. For tight SecVTX tagger the scale factor is 0.96 ± 0.05 [54]. For JetProb tagger ($<$ 5% operating point) the Data/MC scale factor measured in CDF is 0.77 ± 0.04. The scale factors that are actually used, labeled SS', SJ', 1S', are defined as:

- SS' = 0.92 × $\mathrm{N_{SS}}$
- SJ' = 0.74 × $\mathrm{N_{SJ}}$ + 0.05 × $\mathrm{N_{SS}}$
- 1S' = 0.96 × $\mathrm{N_{1S}}$ + 0.22 × $\mathrm{N_{SJ}}$ + 0.03 × $\mathrm{N_{SS}}$

Where $\mathrm{N_{1S}}$, $\mathrm{N_{SJ}}$ and $\mathrm{N_{SJ}}$ are the uncorrected predicted rates before applying any scale factor. We then define two different systematics, one for the SecVTX tagger, the other one for the JetProb tagger, based on the uncertainties reported in [54]. These two uncertainties were considered in order to take into account the correlation between the different tagging categories:

- SecVTX: 1S' $=\pm 5.2\%$, SS' $=\pm 10.4\%$, SJ' $=\mp 3\%$
- JetProb: 1S' $=\mp 3\%$, SS' $=\pm 0\%$, SJ' $=\pm 3.3\%$

Trigger efficiency The trigger efficiency study is described in [55]. We assign a systematic uncertainty to both MC-based backgrounds and signal acceptances by varying the trigger efficiency by $\pm 1\sigma$.

Lepton veto The uncertainty in the efficiency of these cuts was determined to be safely accounted for by assuming ±2% [45].

ISR/FSR The uncertainty associated with the initial and final state radiation was evaluated for the signal by generating samples with more/less ISR/FSR. Up to this point in the analysis, this uncertainty is applied only to single top.

TRF There is an uncertainty in the Tag Rate Function parameters. The variations in the Tag Rate Matrix, which is used to estimate the QCD multijet background, modify the distributions as well. This taken into account by varying the tag-rate probability in each bin of the matrix by $\pm 1\sigma$, and the alternative shapes are used in the limit calculation. This is only considered for the QCD multijet background.

A summary of systematic uncertainties for background processes is given in table 6.1.

Systematic	Region	single top	diboson	$t\bar{t}$	V+jets	QCD
Lumi	1S +SJ +SS	$\pm^{6\%}_{6\%}$	$\pm^{6\%}_{6\%}$	no	no	no
PDF	1S +SJ +SS	$\pm^{2\%}_{2\%}$	$\pm^{2\%}_{2\%}$	no	no	no
Lepveto	1S +SJ +SS	$\pm^{2\%}_{2\%}$	$\pm^{2\%}_{2\%}$	no	no	no
SB-tag	1S	$\pm^{5.2\%}_{5.2\%}$	$\pm^{5.2\%}_{5.2\%}$	$\pm^{5.2\%}_{5.2\%}$	no	no
	SJ	$\mp^{3\%}_{3\%}$	$\mp^{3\%}_{3\%}$	$\mp^{3\%}_{3\%}$	no	no
	SS	$\pm^{10.4\%}_{10.4\%}$	$\pm^{10.4\%}_{10.4\%}$	$\pm^{10.4\%}_{10.4\%}$	no	no
JB-tag	1S	$\mp^{3\%}_{3\%}$	$\mp^{3\%}_{3\%}$	$\mp^{3\%}_{3\%}$	no	no
	SJ	$\pm^{3.3\%}_{3.3\%}$	$\pm^{3.3\%}_{3.3\%}$	$\pm^{3.3\%}_{3.3\%}$	no	no
	SS	$\mp^{0\%}_{0\%}$	$\mp^{0\%}_{0\%}$	$\mp^{0\%}_{0\%}$	no	no
XSEC	1S +SJ +SS	$\pm^{15\%}_{15\%}$	$\pm^{6\%}_{6\%}$	$\pm^{6.6\%}_{6.6\%}$	no	$\pm^{1\%/6\%/7\%}_{1\%/6\%/7\%}$
JES s/r	1S	yes/$\pm^{4\%}_{4\%}$	yes/$\pm^{6\%}_{6\%}$	yes/$\mp^{2\%}_{2\%}$	yes/no	no/no
	SJ	yes/$\pm^{4\%}_{4\%}$	yes/$\pm^{5\%}_{5\%}$	yes/$\pm^{1\%}_{1\%}$	yes/no	no/no
	SS	yes/$\pm^{3\%}_{3\%}$	yes/$\pm^{6\%}_{6\%}$	yes/$\pm^{1\%}_{1\%}$	yes/no	no/no
Q^2	1S +SJ +SS	no	no	no	yes (only Wj)	no
TRF	1S +SJ +SS	no	no	no	no	yes
ISR/FSR	1S +SJ +SS	$\pm^{2\%}_{2\%}$	no	no	no	no
Trigger	1S +SJ +SS	$\pm^{2\%}_{2\%}$	$\pm^{2\%}_{2\%}$	$\pm^{2\%}_{2\%}$	no	no

Table 6.1 – A summary of the systematic uncertainties associated with each background process.

6.4 Results

The multichannel fit procedure is applied to the $M_T(\not{E}_T, j_{1,2,3})$ distribution. Since no excess above SM prediction is present, 95% CL limits are extracted. To obtain the upper limit s_u, the marginalized posterior is integrated over s using numerical integration. To obtain expected limits, the procedure is iterated on an ensemble of M pseudoexperiments, and the results are then averaged over M.

The procedure must be repeated for each $M_{W'}$ point in the range of interest, and then compared to the theoretical cross-section for W' production to interpret the results in terms of an excluded $M_{W'}$ range. Computing-wise fixme, the procedure is extremely time-intensive, as both a high density of points in the systematics space and a high number of iterations (in our analysis, $M = 10000$) are necessary to fulfill convergence requirements and ensure satisfactory results [53]. At the moment of writing, the calculations for the mass points in the range $300 \leq M_{W'} \leq 900$ GeV are being performed [56].

The observed and expected limits for $M_{W'}$ = 200 GeV are reported in table 6.2.

$M_{W'}$ (GeV/c^2)	$\sigma \times \mathcal{B}$ (pb)	95% CL limit (obs)	95% CL limit (exp) $\pm 1\sigma$
200	39.43	1.73	$1.71^{+0.88}_{-0.68}$

Table 6.2 – W' mass points and corresponding 95% CL expected and observed limits.

Conclusions

In this thesis, a search for W' production in events with large missing transverse energy and jets was reviewed. The theoretical background was reported in Chapter 1, with a brief description of the Standard Model and possible minimal extensions, including a benchmark W' model. The experimental setup was described in Chapter 2: the `CDF` experiment as it was during the Run II. In Chapters 3, 4, 5 the main features of the analysis were presented: starting from the reconstruction of the physical objects to the description of the analysis strategy, the event selection, the background rejection and the final discriminant used to fit for W' signal. In the last Chapter the fitting procedure and the first limit at $M_{W'}$ = 200 GeV are shown. Since no excess above SM predictions is found, 95% CL upper limits on $\sigma(p\bar{p} \to W') \times \mathcal{B}(W' \to tb)$ are placed for a W' boson of mass $M_{W'}$ = 200 GeV.

At this point in time (Spring 2013) the analysis is still in progress. The limits for the other mass points up to 900 GeV are to be set in the next weeks. The first results, that are the main object of this thesis work, have already been presented to the `CDF` Top/BSM (Beyond the Standard Model) analysis group, and the main parts of the analysis have already been approved.

The current plan is to come up with a full set of limits by the end of June. In the meantime, the same analysis in the lepton plus jets sample is going to be finalized. The first comparison between the two analyses will be fundamental in order to see if further improvement is needed, especially in the search for more elusive resonances in the tb final state. A number of tools have already been developed and tested for the single top s-channel search in both the missing transverse energy plus jets and lepton plus jets analyses, and their use in the W' analyses are under consideration. During the Summer a task force, that is going to include new students, is going to be formed to work on the finalization of searches for New Physics in the tb final states. The goal of the `CDF` collaboration is to produce a final answer on W' and charged Higgs production, in the mass range below about 1 TeV$/c^2$, by the end of the Summer 2013.

Bibliography

[1] ATLAS Collaboration, *Observation of a new particle in the search for the Standard Model Higgs boson with the ATLAS detector at the LHC*, Phys.Lett. B716 (2012) 1-29

[2] CMS Collaboration, *Observation of a new boson at a mass of 125 GeV with the CMS experiment at the LHC*, Phys. Lett. B 716 (2012) 30-61

[3] I. J. R. Aitchison and A. J. G. Hey. *Gauge Theories in Particle Physics: A Practical Introduction*. Adam Hilger, 1989.

[4] K. Nakamura et al. Review of particle physics. *J. Phys.*, G37, 2010.

[5] Ahmad et al. Direct evidence for neutrino flavor transformation from neutral-current interactions in the Sudbury neutrino observatory. *Phys. Rev. Lett.*, 89, 2002.

[6] Y. et al. Fukuda. Evidence for oscillation of atmospheric neutrinos. *Phys. Rev. Lett.*, 81, 1998.

[7] G. Shaw F. Mandl. *Quantum field Theory*. John Wiley and Sons, 1984.

[8] E. Fermi. *Nuovo Cim.*, 1 (11), 1934.

[9] S. L. Glashow. Partial Symmetries of Weak Interactions. *Nucl. Phys.*, 22:579–588, 1961.

[10] P.W. Higgs. Broken symmetries, massless particles and gauge fields. *Physics Letters*, 12(2), 1964.

[11] F. Englert and R. Brout. Broken symmetry and the mass of gauge vector mesons. *Phys. Rev. Lett.*, 13:321–323, Aug 1964.

[12] G. S. Guralnik, C. R. Hagen, and T. W. B. Kibble. Global conservation laws and massless particles. *Phys. Rev. Lett.*, 13:585–587, Nov 1964.

[13] S. Weinberg. A model of leptons. *Phys. Rev. Lett.*, 19:1264–1266, 1967.

[14] A. Salam. *Elementary Particle Theory*. Almqvist and Wiksells, Stockholm, 1968.

[15] Y. Mimura, S. Nandi, Phys. Lett. B **538**, 406 (2002); G. Burdman, B. Dobrescu, E. Ponton, Phys. Rev. D **74**, 075008 (2006).

[16] E. Malkawi, T. Tait, C.P. Yuan, Phys. Lett. **385**, 304 (1996); H. Georgi, E. Jenkins, E. Simmons, Nucl. Phys. B **331**, 541 (1990).

[17] M. Perelstein, Prog. Part. Nucl. Phys. **58**, (2007).

[18] J.C. Pati, A. Salam, Phys. Rev. D **10**, 275 (1974); R.N. Mohapatra, J.C. Pati, Phys. Rev. D **11**, 566 (1975); G. Senjanovic, R.N. Mohapatra, Phys. Rev. D **12**, 1502 (1975).

[19] CDF Collaboration, *Search for the Production of Narrow tb Resonances in 1.9 fb*$^{-1}$ *of* $p\bar{p}$ *Collisions at* $\sqrt{s} = 1.96$ *TeV*, PRL 103, 041801 (2009)

[20] Z. Sullivan, *Fully differential* W' *production and decay at next-to-leading order in QCD*, Phys. Rev. D **66** (2002)

[21] CDF Collaboration, *Search for Resonant Top-Antitop Production in the Lepton Plus Jets Decay Mode Using the Full CDF Data Set*, Phys. Rev. Lett. 110, 121802 (2013).

[22] R. M. Harris and S. Jain, *Cross Sections for Leptophobic Topcolor Z′ Decaying to Top-Antitop*, Eur. Phys. J. C **72**, 2072 (2012)

[23] D0 Collaboration, *Search for charged Higgs bosons decaying to top and bottom quarks in $p\bar{p}$ collisions*, Phys. Rev. Lett. **102**, 191802 (2009)

[24] C. M. Ginsburg, "Cdf run 2 muon system," *The European Physical Journal C - Particles and Fields*, vol. 33, pp. s1002–s1004, 2004. 10.1140/epjcd/s2004-03-1795-6.

[25] G. Ascoli *et al.*, "Central Muon Level-1 Trigger Electronics," FERMILAB-PUB-87-188-E.

[26] D. Mohl, "Physics and technique of stochastic cooling," *Phys. Reports*, vol. 58, 1980.

[27] I. Vila, "Performance and First Physics Results of the SVT Trigger at CDF II," *ArXiv High Energy Physics - Phenomenology e-prints*, jul 2003.

[28] B. Ashmanskas *et al.*, "The CDF Silicon Vertex Trigger," *Nuclear Instruments and Methods in Physics Research A*, vol. 518, pp. 532–536, Feb. 2004.

[29] T. Affolder *et al.*, "CDF central outer tracker," *Nucl. Instrum. Meth.*, vol. A526, pp. 249–299, 2004.

[30] D. Acosta et al. (CDF Collaboration) *A Time-Of-Flight Detector in CDF II* Nucl. Instrum. Meth. A518 (2004) 605.

[31] `http://www-cdf.fnal.gov/cdfsim/validation/cot/cotVal.html`.

[32] R. Blair *et al.*, "The CDF-II detector: Technical design report," FERMILAB-DESIGN-1996-01.

[33] P. Gatto, "Performance of the new tracking system at CDF II," Master's thesis, University of Padova, 2001.

[34] S. Menzemer, "A tracking and alignment software package for the CDF II silicon detector," Master's thesis, University of Karlsruhe, 2002.

[35] F. D. Snider, *Tracking at CDF: Algorithms and experience from Run I and Run II*, Nuclear Instruments and Methods in Physics Research A, vol. 566, pp. 133–141, Oct. 2006.

[36] K. Nakamura *et al.*. (Particle Data Group) J. Phys. G **37** (2010) 075021.

[37] G.C. Blazey *et al.*. *Run II Jet Physics* CDF Note 5293

[38] F. Abe *et al.*. (CDF Collaboration) *The Topology of Three Jet Events in* $p\overline{p}$ *Collisions at* $\sqrt{s}$ *= 1.8 TeV* Phys. Rev. D 45 (1992) 1448.

[39] A. Bhatti *et al.*. (CDF Collaboration) *Determination of the Jet Energy Scale at the Collider Detector at Fermilab* Nucl. Instrum. Meth.A566 (2006) 375.

[40] W. Ketchum, V. Rusu, M. Trovato, *New Jet Energy Scale Corrections for Quarks and Gluons*, CDF Note 10829

[41] T. Sjostrand *et al.*., *High-Energy-Physics Event Generation with PYTHIA 6.1*, Comput. Phys. Commun. 135 (2001) 238.

[42] D. Gerdes, *B Identification Using Jet Probability*, CDF Note 2023

[43] J. Freeman, *SecVTX Scale Factors Calculated Using the Electron Method Through Period 22*, CDF Note 9848

[44] Q. Liu, K. Potamianos, F. Margaroli, D. Bortoletto, *Background Estimation in MET + b-Jets Analysis*, CDF Note 10452

[45] A. Apresyan *et al.*, *Event selection for Higgs search in the* $\not{E}_T$ *plus jets sample*, CDF Note 9358

[46] J. Therhaag [TMVA Core Developer Team Collaboration], *TMVA: Toolkit for multivariate data analysis*, AIP Conf. Proc. **1504**, 1013 (2009).

[47] E. Thomson *et al..*, *Combination of CDF and D0 $t\bar{t}$ Cross-sections*, CDF note 10916

[48] S. Jindariani, S. Klimenko, J. Konigsberg, G. Lungu, V. Necula, L. Pinera, A. Pronko, R. Rossin, A. Sukhanov, D. Tsybychev, S.M. Wang, Luminosity Uncertainty for Run 2 up until August 2004, CDF Note 7446

[49] Oscar Gonzalez, Carsten Rott, Uncertainties due to the PDFs for the gluino-sbottom search, CDF Note 7051

[50] C. Rott, at al. CDF Note 7136, Search for Scalar Bottom Quarks from Gluino Decays in Proton-Antiproton Collisions at 1.96 TeV, PhD Thesis, CDF Note 7526.

[51] A. Mehta, Calibration of H1 Algorithm Improved Jets, CDF Note 8564, 2006

[52] M. L. Mangano *et al.*, ALPGEN, a generator for hard multiparton processes in hadronic collisions, J. High Energy Phys. 0307 (2003) 001

[53] Sensitivity, Exclusion and Discovery with Small Signals, Large Backgrounds, and Large Systematic Uncertainties, CDF Note 8128

[54] V. Giakoumopoulou, J. Freeman, *Summer 2010 SevVtx Scale Factors Calculated Using the Electron Method through Period 28*, CDF Note 10178

[55] O. Gonzalez and M. Vidal, Getting ready for the 4 fb^{-1} dataset: Trigger efficiency of the MET+JETS samples, CDF Note 9745

[56] M. Casarsa *et al.*, *The CDF CAF User's Guide*, CDF Note 6092

Acknowledgments

The work described in this thesis would not have been possible without the people who guided and supported me during the time I spent at Fermilab and in Rome. I try to express my gratitude in the best way I can on this page: `http://www-cdf.fnal.gov/~ludobian/acknowledgments.html`.

Ringraziamenti

È assolutamente certo che senza le persone che mi hanno accompagnato e sostenuto durante il mio percordo di studi non sarei mai riuscito ad arrivare fin qui; per questo motivo, è quasi impossibile riuscire a esprimere in poche parole la mia gratitudine per loro nel modo in cui meriterebbero. Provo a farlo in questa pagina: `http://www-cdf.fnal.gov/~ludobian/ringraziamenti.html`.